THE GROWTH OF METASTABLE PERITECTIC COMPOUNDS

Annual Report

on

Contract NAS8-32998

by

David J. Larson, Jr.

and

Ron G. Pirich

Materials and Structural Mechanics

Research Department

Grumman Aerospace Corporation

Bethpage, New York 11714

and

W.R. Wilcox

Chemical Engineering Department

Clarkson College of Technology

Potsdam, New York 13676

January 1981

Prepared for

George C. Marshall Space Flight Center

Marshall Space Flight Center, Alabama 35812

Grumman Research Department Memorandum RM-714

THE GROWTH OF METASTABLE PERITECTIC COMPOUNDS

by

David J. Larson, Jr.

and

Ron G. Pirich

Materials and Structural Mechanics

Research Department

Grumman Aerospace Corporation

Bethpage, New York 11714

and

W.R. Wilcox

Chemical Engineering Department

Clarkson College of Technology

Potsdam, New York 13676

Annual Report on Contract NAS 8-32998

January 1981

Approved by: Richard A. Scheuing
Director of Research

CONTENTS

ILLUSTRATIONS

NOMENCLATURE

D - Diffusion coefficient in melt (m^2/s)

g - Mass fraction solidified

g_I - Fraction solidified when $w_i = w_{ip}$, beyond which two-phase $\alpha + \beta$ is produced.

g_{II} - Mass fraction solidified when $w_s = w_{\beta p}$, beyond which single-phase β is produced.

g_e - Mass fraction solidified for $w_s = w_{\beta e}$, beyond which two-phase $\beta + \gamma$ is produced.

k - Distribution coefficient: $k = w_s/w_i$

k_α - Distribution coefficient for single-phase α region

k_β - Distribution coefficient for single-phase β region

k_{eff} - Effective distribution coefficient: $k_{eff} = w_s/w_\ell$

L - Length of melt (m)

t - Time for initiation of solidification (s)

V - Solidification rate (m/s)

V_{cf} - Crystallization flow due to solidification (m/s): $V_{cf} = V\zeta_s/\zeta_\ell$

w - Mass fraction composition in melt at distance y from interface

w_e - Eutectic composition, mass fraction

w_i - Interfacial melt composition, mass fraction

w_{ip} - Peritectic melt composition, mass fraction

w_ℓ - Average melt composition, mass fraction

$w_{\ell I}$ - Bulk melt composition when $w_i = w_{ip}$

w_o - Initial composition of feed, mass fraction

w_s - Average composition of solid at a point, taken to be in equilibrium with w_i when formed (see w_α, w_β)

w_α - Composition of α on solidus

$w_{\alpha p}$ - Composition of peritectic α

w_β - Composition of β on solidus

$w_{\beta p}$ - Composition of peritectic β

W - Mass of feed (kg)

y - Distance into melt from interface (m)

z - Distance down solidified ingot (m)

z_I - Distance at which $w_i = w_{ip}$

δ - Thickness of fictitious stagnant film (m)

ρ_ℓ - Density of melt (kg/m^3)

ρ_s - Density of solid (kg/m^3)

ABSTRACT

In this program the influence of gravitationally driven thermosolutal convection on the directional solidification of peritectic alloys is being studied. The relationships between the solidification processing conditions, and the microstructure, chemistry, and magnetic properties of peritectic alloys are being investigated. Initially, the Pb-Bi peritectic is being studied as a model solidification system. Completion of the Pb-Bi study, development of a peritectic solidification model, and development of Sm-Co processing and characterization techniques will all contribute to our investigation of Sm-Co peritectic solidification.

Analysis of directionally solidified Pb-Bi peritectic samples indicates that appreciable macrosegregation occurs due to thermosolutal convection and/or Soret diffusion. A peritectic solidification model which accounts for partial mixing in the liquid ahead of the planar solidification interface and describes macrosegregation has been developed.

Two-phase dendritic and banded microstructures have been grown in the Pb-Bi peritectic system. In addition, refined two-phase microstructures have been observed and candidate formation mechanisms proposed.

Material handling, containment, casting, microstructural and magnetic characterization techniques have been developed for the Sm-Co system. Alloys produced with these procedures have been homogeneous. Modifications of these techniques will be used to directionally solidify and characterize Sm-Co peritectic alloys.

1. INTRODUCTION

Many important materials solidify via a peritectic reaction. These include most Cobalt-base superalloys, metal (M) rare earth (RE) magnetic compounds (notably M_5RE and $M_{17}RE_2$), and A_3B superconductors. Single crystals or aligned fibrous composites are desirable morphologies for these materials. Current processing techniques have not produced aligned fibrous composites. Plane-front directional solidification has been shown to produce composite morphologies for eutectic and off-eutectic reactions and, as a consequence, this approach is an attractive candidate for processing peritectics. However, the anticipated two-phase fibrous microstructures have not yet been realized experimentally.

Chalmers (Ref. 1) was the first to anticipate the results that might be obtained from steady state plane-front directional solidification of peritectics. Negligible diffusion in the solid and liquid mixing solely by diffusion was assumed. With respect to the peritectic reaction shown in Figure 1 and for hypoperitectic alloys, i.e., $C_\alpha^P < C < C_\beta^P$, Chalmers predicted a steady state consisting of simultaneous growth of α and β phases, producing a eutectic-like microstructure. Further, he predicted that hypoperitectic alloys ($C_\beta^P < C < C_L^P$) would initially solidify α phase and β would form when the liquid composition at the solidification interface reached C_L^P.

Uhlmann and Chadwick (Ref. 2) were the first to directionally solidify hypoperitectic alloys to examine Chalmer's predictions. They observed that the steady state structures of all hypoperitectic alloys consisted of dendrites of the properitectic α phase in a matrix of peritectic β phase. The range of growth conditions was limited, however, and Chalmers (Ref. 3) subsequently postulated that growth at higher ratios of thermal gradient to solidification velocity might lead to cooperative growth, similar to that found in offeutectic systems. This view was analytically supported by Livingston (Ref. 4), and Flemings (Ref. 5).

Boettinger (Ref. 6) tested these hypotheses experimentally and analytically on the Sn-Cd system, with the following results: adaptation of the constitutional supercooling criteria to the peritectic case approximately predicts an upper bound to the ratio of thermal gradient to solidification velocity (G/V) at which non-planar (dendritic or cellular) growth occurs for hypopertectic alloys; no coupled,

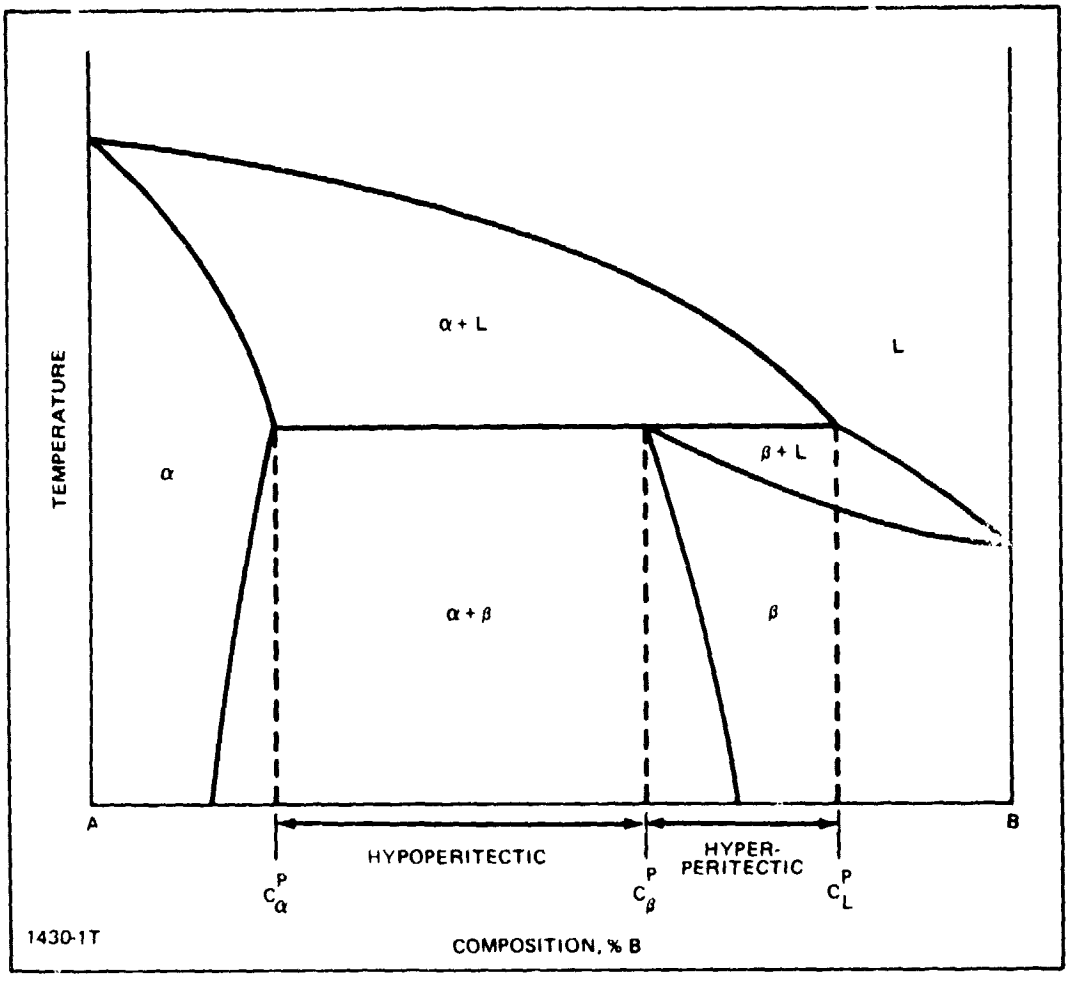

Figure 1 Typical Peritectic Phase Diagram

eutectic-like growth was observed; those samples solidified at a G/V ratio in excess of that required by the constitutional supercooling criteria solidified with a planar interface but with a structure characterized by alternating bands of α and β arrayed perpendicular to the growth direction; an analysis similar to the Jackson and Hunt (Ref. 7) theory for lamellar eutectic growth was performed for a two-phase lamellar peritectic and the undercooling vs. velocity and lamellar spacing was found to be greatly different for the peritectic case. This difference possibly precluded coupled growth in peritectic systems.

Titchener and Spittle (Ref. 8) reached similar conclusions from experiments they conducted on the Zn-Cu system. In addition, they noted macrosegregation in a thermally stabilized geometry for a (Zn-Cu) system presumed to exhibit density-driven thermosolutal convection, whereas they found no evidence of macrosegregation in a Sn-Sb nonconvecting system. Further, they suggest that

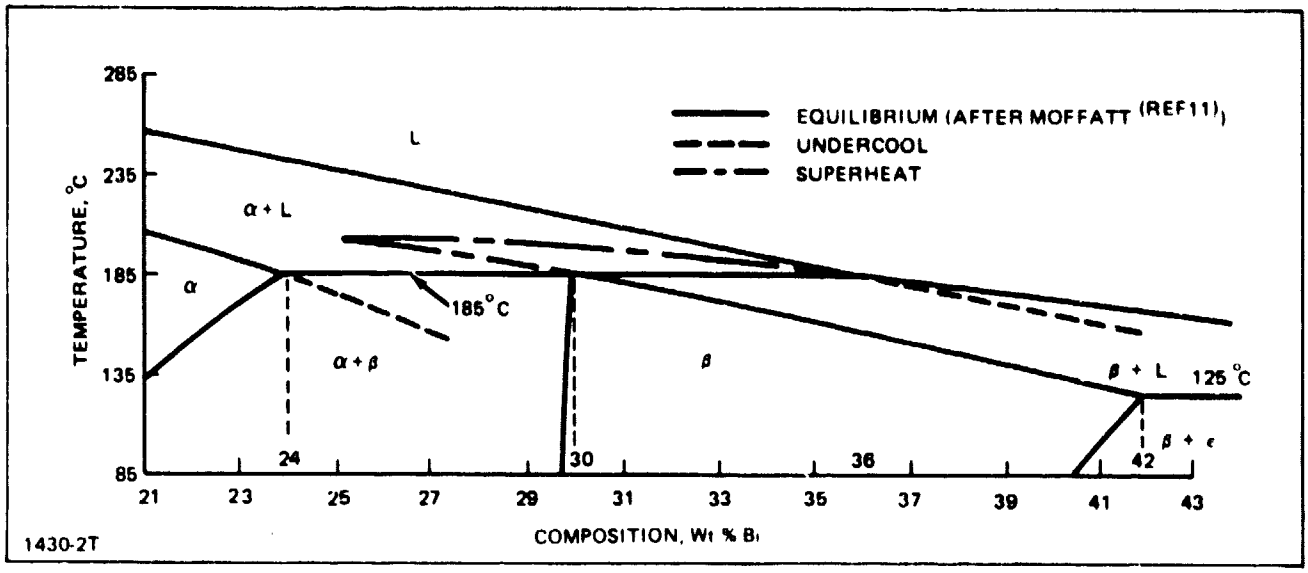

Figure 2 Pb-Bi Peritectic Phase Diagram Segment with Proposed Metastable Solidification Reactions

the alternating planar band structure ceases when the bulk liquid composition, C_L, reaches the liquidus composition, C_L^P, of the peritectic isotherm, T_P.

An additional consideration, that of non-equilibrium peritectic transformation, was introduced by Kerr, Cisse, and Bollings (Ref. 9) and Shcherbakov, David and Brody (Ref. 10). The former suggest that, in addition to the equilibrium peritectic reaction, there is also the possibility of suppression of the peritectic transformation by either supersaturation of the properitectic phase in solute and undercooling or a non-equilibrium peritectic reaction above the peritectic isotherm, i.e., superheating. These possibilities are shown schematically in Figure 2 for the Pb-Bi peritectic reaction under investigation. Both were shown to be energetically favorable; that is, solidification occurs with a net reduction in free energy. Kerr, Cisse, and Bollings (Ref. 9) offer support for the superheat mechanism for high-rate dendritic solidification of Al-Ti alloys. Scherbakov, David and Brody (Ref 10) also support the superheat mechanism for plane-front solidification of hypoperitectic Pb-Bi alloys, although they made no measurement of local compositions.

The present program was initiated to investigate mechanisms encountered during plane front directional solidification of peritectic alloys and determine whether these mechanisms or morphologies were significantly influenced by gravitationally driven thermosolutal convection. The Bridgman-Stockbarger solidification technique was selected.

The model alloy system selected for the initial study was Pb-Bi. This peritectic system was selected because of similarities with the Sm-Co peritectic system and the relative ease of processing. We will investigate the Sm-Co system later in the program. Similarities include the compositional extent of the peritectic isotherm (12 wt.% Sm or Bi) and similar liquidus slopes at the peritectic isotherm (7.313°C/a.% Bi for Pb-Bi and 8.62°C/a.% Sm for Sm-Co). This results in interface stabilization requirements (G/V) that are comparable in magnitude. The Pb-Bi peritectic, however, occurs in a temperature range (125 - 325°C) that is easily achieved and the melt is passive to our stainless steel sheathed thermocouple probes, so we can make reliable in-situ thermocouple measurements at the solidification interface. In the first year, we planned to focus on the directional solidification of the Pb-Bi model system and the development of handling, processing, and analysis techniques for the Sm-Co system.

2. EXPERIMENTAL TECHNIQUES

2.1 Pb-Bi SYSTEM

2.1.1 Alloy Preparation

Starting Pb and Bi materials were 99.999% pure. Initially, alloys were resistance melted at a vacuum of 5×10^{-5} Torr for three nours at 450°C in one-half in. diameter alumina crucibles and were then allowed to furnace cool. However, there was severe gravitationally driven segregation of the Bi to the top of the ingots and the alloys were discarded. The next attempt used induction melting in an evacuated quartz ampoule for three to four hours at 600°C, using electromagnetic stirring for homogenization, and drop-quenching the ampoule in a bath of iced water. Unfortunately, the ampoule exploded and the alloy was destroyed. Finally, induction melting and homogenization was used and the molten alloy was allowed to cool slowly in the evacuated quartz ampoule. This produced ingots that were quite homogeneous in the vicinity of the peritectic composition (34.4 ± 0.4 a.%) (Ref. 11) but that had increasing levels of macrosegregation as the temperature differential between the liquidus and solidus temperatures increased. As a result, the starting material should be carefully selected from the length of the ingot, in order to minimize nonuniformity. Chemical spectrophotometric analysis was performed on each end of the selected segments and the level of macrosegregation was restricted to less than 1% of the nominal composition. Alloys of 20, 24, 28, 32, 36 and 40 wt.% Bi were prepared.

2.1.2 Directional Soldification

The ampoule design for directional solidification is shown in Figure 3. The ampoules were intrumented with one Omega Engineering SCASS-010G 16 ultra-fine chromel alumel thermocouple probe. These probes consist of 0.0005 in. thermocouple wires packed with MgO insulation in a 0.010 in. stainless steel sheath.

Ampoules were processed in a directional solidification furnace. The furnace is shown schematically in Figure 4. It is a resistance-heated Bridgman-Stockbarger furnace with active cooling in the chill block. Solidification velocity may be varied from 0.1 to 150 cm/hr. Temperature profiles over a range of power conditions are also shown in Figure 4. Thermal gradients were typically varied from 100 to 300°C/cm and solidification velocities were varied from 0.1 to 1 cm/hr in this study.

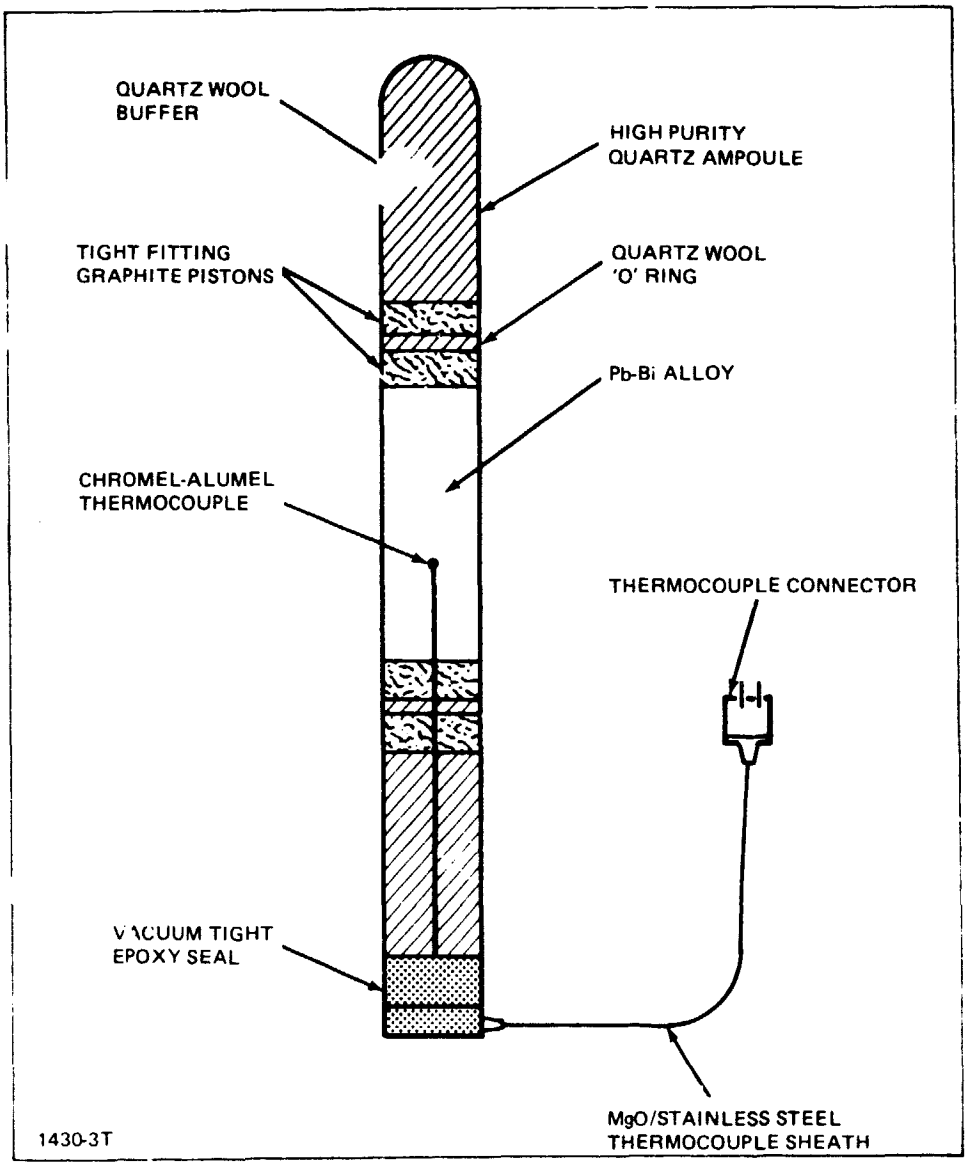

Figure 3 Ampoule Design for Directional Solidification

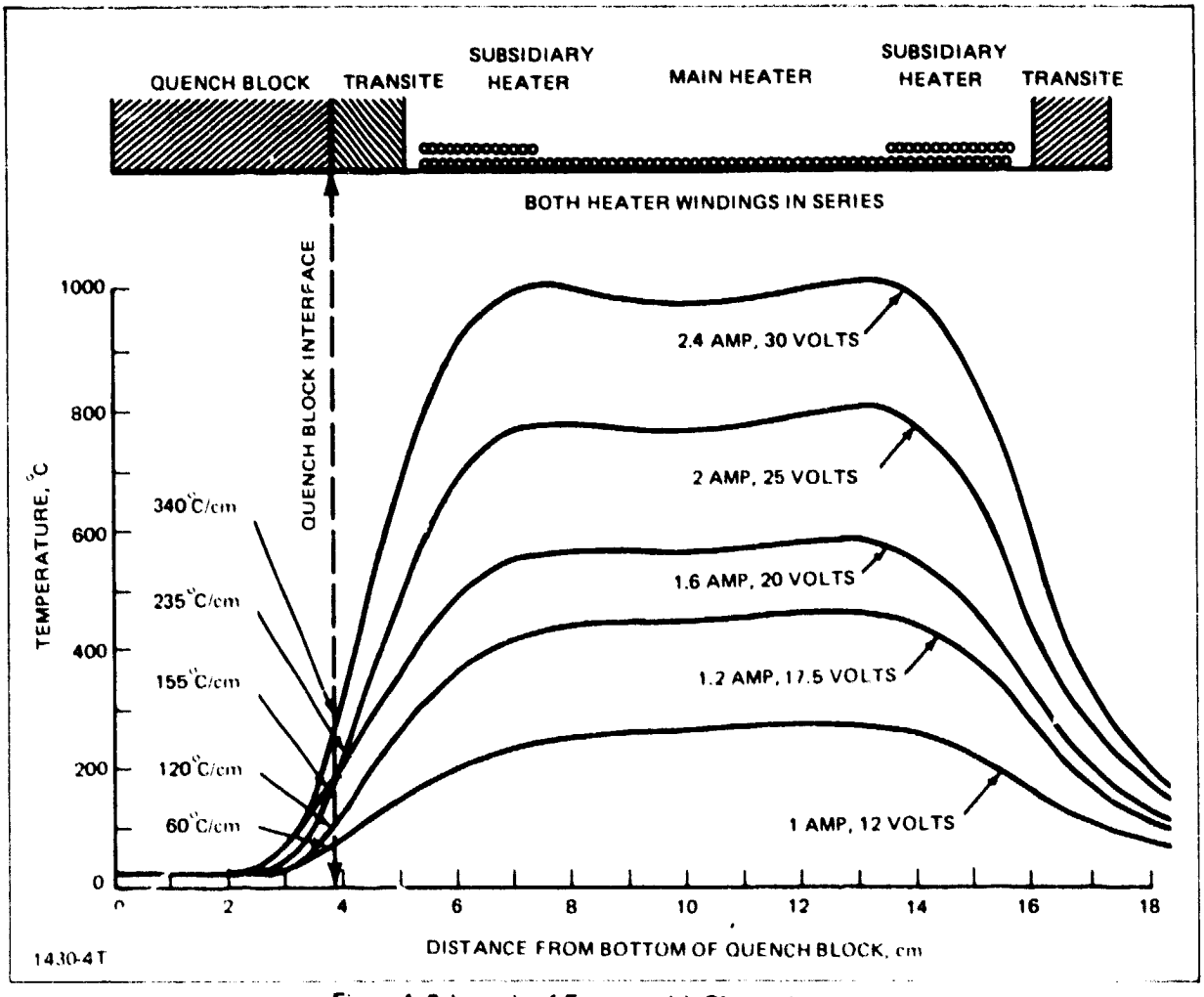

Figure 4 Schematic of Furnace with Observed Temperature Profiles

The temperature/time behavior during solidification was monitored using a Digitec digital thermocouple monitoring system. The temperature vs. time output was analyzed to determine the cooling rate in the solid and liquid and the solidification temperature. The thermal gradient in the solid and liquid were then calculated by dividing the cooling rate by the solidification velocity. It was assumed that the solidification velocity was identical to the furnace translation velocity. The alloys that were directionally solidified, and their growth conditions, are summarized in Table 1. The growth conditions shown in Table 1 were assumed to apply over the entire sample length, although macrosegregation and concomitant solidification temperature variation might seriously compromise this assumption.

TABLE I SAMPLE PROCESSING CONDITIONS

NOMINAL COMPOSITION, Wt. % Bi	SOLIDIFICATION VELOCITY, cm/HR	THERMAL GRADIENT, °C/cm	G/V °C s/cm²	GROWTH DIRECTION
20	0.26±0.05	255±25	3.53±0.76	UP
24	0.95±0.20	256±25	0.97±0.23	UP
24	0.47±0.10	253±25	1.94±0.42	UP
28	0.34±0.07	264±25	2.80±0.63	UP
28	0.17±0.03	252±25	5.34±1.19	UP
28	0.18±0.04	248±25	4.96±1.11	UP
28	0.30±0.06	263±25	3.16±0.70	UP
28	0.22±0.04	118±12	1.93±0.40	DOWN
28	0.20±0.04	122±12	2.20±0.49	DOWN
28	0.12±0.04	159±16	4.85±1.90	DOWN
28	1.05±0.07	79±8	0.27±0.03	DOWN
28	0.83±0.17	155±16	0.67±0.15	DOWN
32	0.83±0.17	252±25	1.09±0.25	UP
32	0.43±0.08	122±12	1.02±0.21	UP
32	0.17±0.03	318±32	6.82±1.51	UP
36	0.17±0.01	255±25	5.28±0.58	UP
40	1.19±0.24	233±23	0.71±0.16	UP

80R-1430-16T

2.2 Sm-Co SYSTEM

2.2.1 Alloy Preparation

An experimental study was conducted to evaluate crucible materials capable of containing molten Sm-Co. Aluminum oxide, boron nitride, graphite, and mullite crucibles were examined. Using 325-mesh Sm powder of 99.9 purity and 325-mesh Co powder of 99.99% purity, a 82.3 a/o Co alloy was first mechanically mixed and then heat treated at 200°C for eight hours in vacuo to remove any residual moisture. This composition corresponds to a slightly Sm-rich $SmCo_5$ stoichiometry. (See the Sm-Co phase diagram in Figure 5.) Using a 450 Hz, 10 kW, rf generator and the crucible shown schematically in Figure 6, this Sm-Co alloy was slowly heated to 1325°C and held for two hours. The temperature was monitored by an optical pyrometer. Both the graphite and mullite crucibles were attacked, and this caused severe contamination of the melt. The aluminum oxide crucible reacted with the melt to a lesser degree, but contamination throughout the melt was considerable. Pyrolized boron nitride, on the other hand, was superior to the other crucible materials studied. There was a discernible reduction of the crucible wall, presumably some SmN phase being formed; however, this reaction product was localized to a very small film at the melt-crucible interface and caused a minimal contamination of the melt. These results are in general agreement with Miller and Austin (Ref. 12) and indicate that pyrolytic boron nitride provides an effective crucible material at the temperatures investigated.

The composition of the solidified product was varied by changing the relative proportions of the starting powders. Unfortunately, Sm has a relatively high vapor pressure (5.4×10^{-2} atm at 1325°C) compared with cobalt (3.8×10^{-7} atm at 1325°C). Therefore, large losses of Sm were observed during melting. For example, starting with an initial composition of $Sm_{17.7}Co_{82.3}$, a final Sm content of 5.4 a/o was found after inductively heating at 1325°C for two hours. The Sm:Co composition was shifted from approximately $SmCo_5$ to the mid-range of Sm_2Co_{17}/Co (see Figure 5). The final composition was determined using energy-dispersive analysis of x-rays (EDAX), electron microprobe spectroscopy and magnetization measurements. The resulting solidified product was macroscopically homogeneous and the melt appears to have been well stirred. In future work a closed crucible geometry will be used which will minimize or eliminate the preferential loss of Sm due to vaporization.

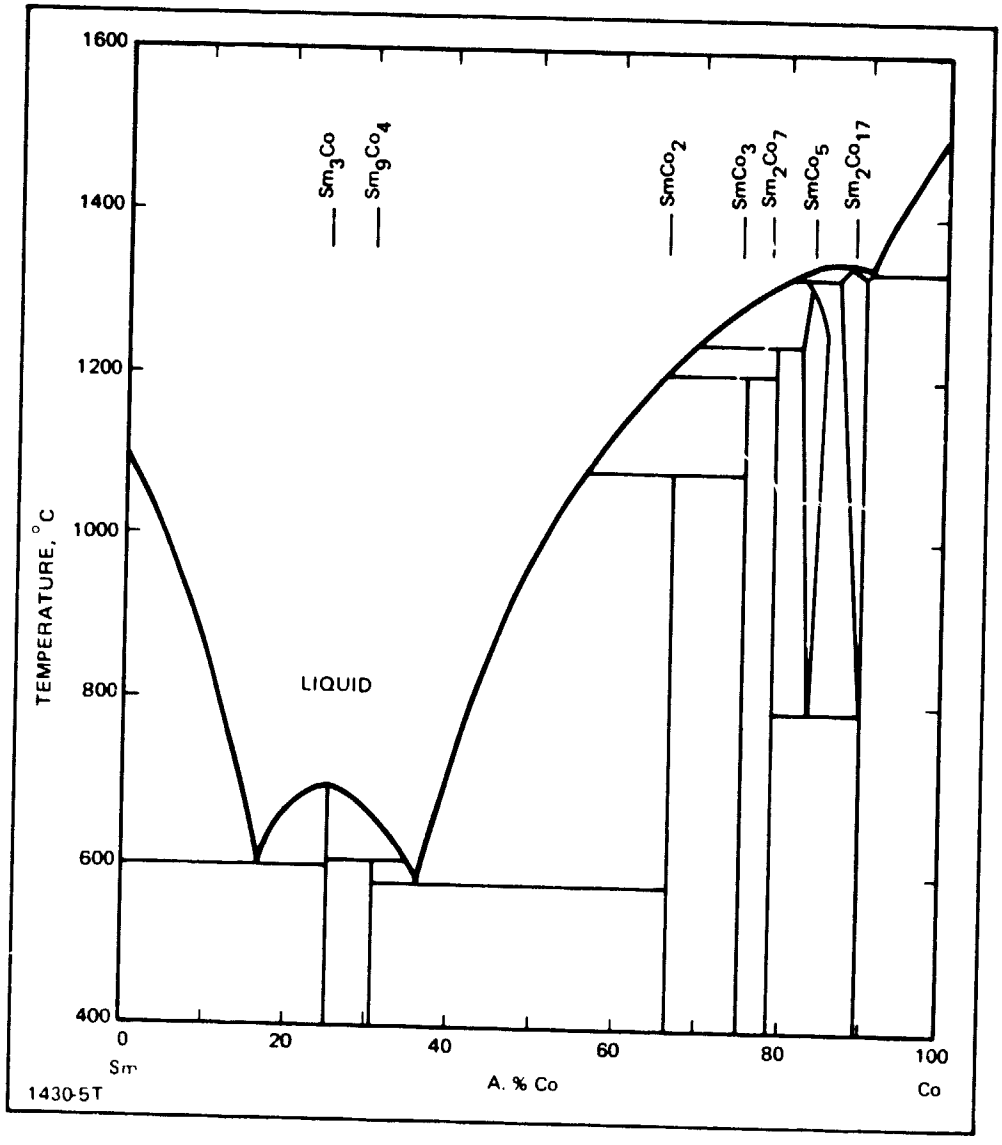

Figure 5 Sm-Co Phase Diagram (Ref. 18)

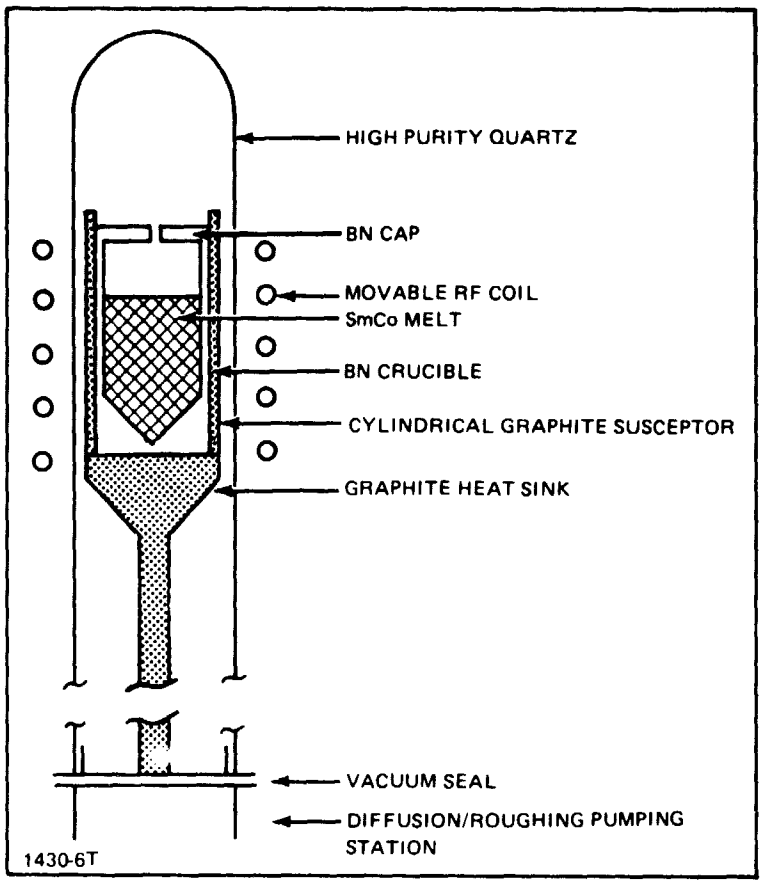

Figure 6 Solidification Apparatus for Growth of Sm-Co Compounds

3. RESULTS AND DISCUSSION

3.1 Pb-Bi SYSTEM

3.1.1 Phase Diagram Evaluation

The Pb-Bi phase diagram was checked using differential scanning calorimetry (DSC). Samples for DSC analysis were segments of directionally solidified ingots that had been chemically analyzed using an electron microprobe. The samples were run in a Dupont 900 Thermal Analyzer in the heating mode, and the temperature differential was monitored between the sample and an aluminum standard from 25 to 350°C. Calibration using pure Pb, In, and Bi allowed the solidus and liquidus temperatures to be determined as a function of composition. These data are shown in Figure 7, superimposed on the most recent Pb-Bi phase diagram (Ref. 11). The agreement is excellent for the temperatures of the peritectic and eutectic reaction isotherms. However, there are differences in the liquidus temperatures which are significant in calculating the constitutional supercooling requirements for plane-front solidification. The hyperperitectic β solidus may also be steeper than previously reported. Insufficient data are available at this time to comment more specifically on the latter point; however, additional samples will be run.

3.1.2 Morphological Stability

The local microstructure of a directionally solidified alloy is a function of both the local composition and the solidification processing parameters at the solidification interface. Variation of either the local composition or the thermal processing parameters as solidification progresses can result in changes in morphology. Typical morphological transformations that were observed in the Pb-Bi peritectic system are shown in Figure 8 a-d. A single-phase to two-phase transition from properitectic α to an $\alpha + \beta$ dendritic array is shown in Figure 8a. This sample was processed at a G/V ratio of $2.8 \times 10^6 \pm .63 \times 10^6$ °C s/cm^2. A two-phase to single phase transition from an $\alpha + \beta$ dendritic array to planar peritectic β is shown in Figure 8b. This sample was processed with a G/V ratio of $1.94 \times 10^6 \pm .42 \times 10^6$ °C s/cm^2. Two banded structures (alternating layers arrayed perpendicular to the solidification direction) were noted and are shown in Figure 8c. Proceeding in the solidification direction, the first two bands shown consist of a non-planar $\alpha + \beta$ dendritic array followed by a layer of planar β.

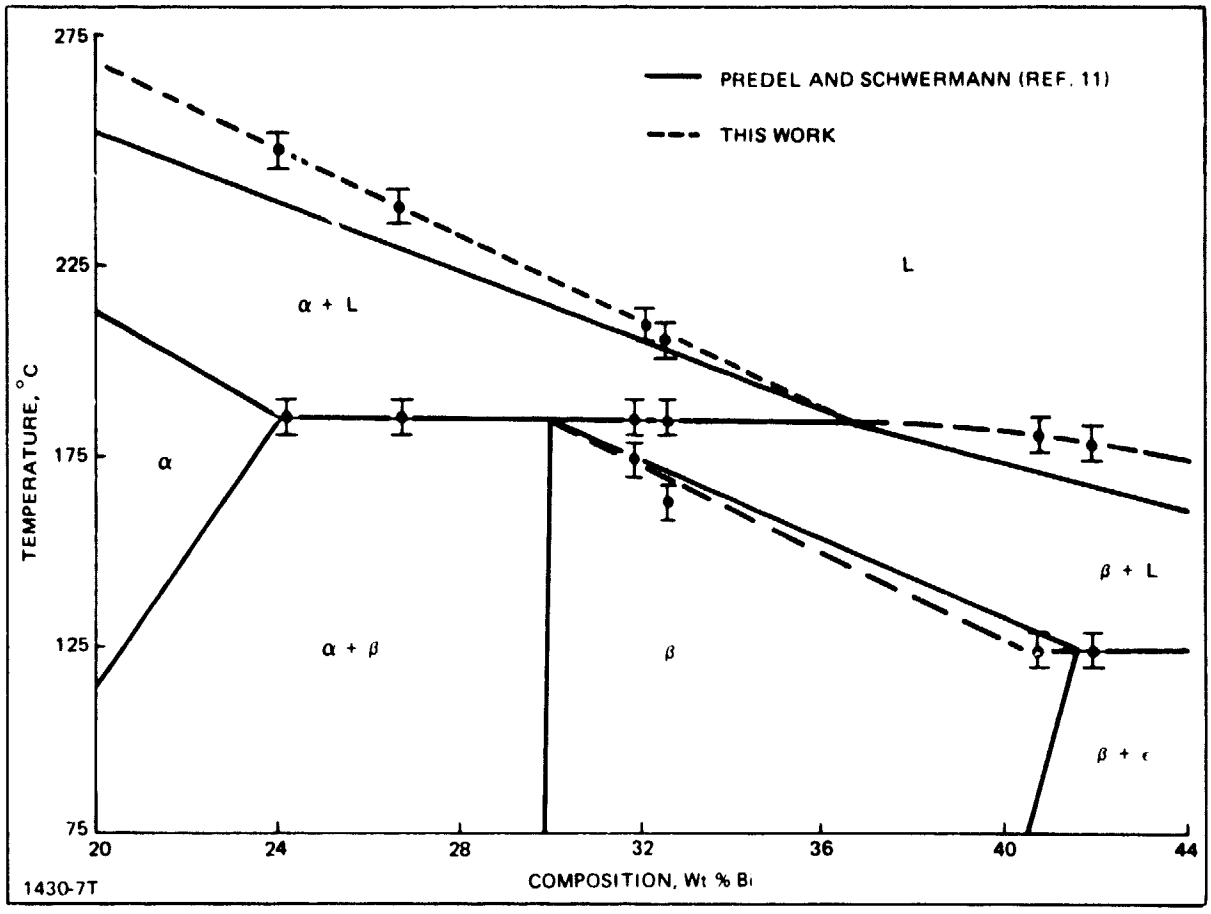

Figure 7 Results of DSC Analysis

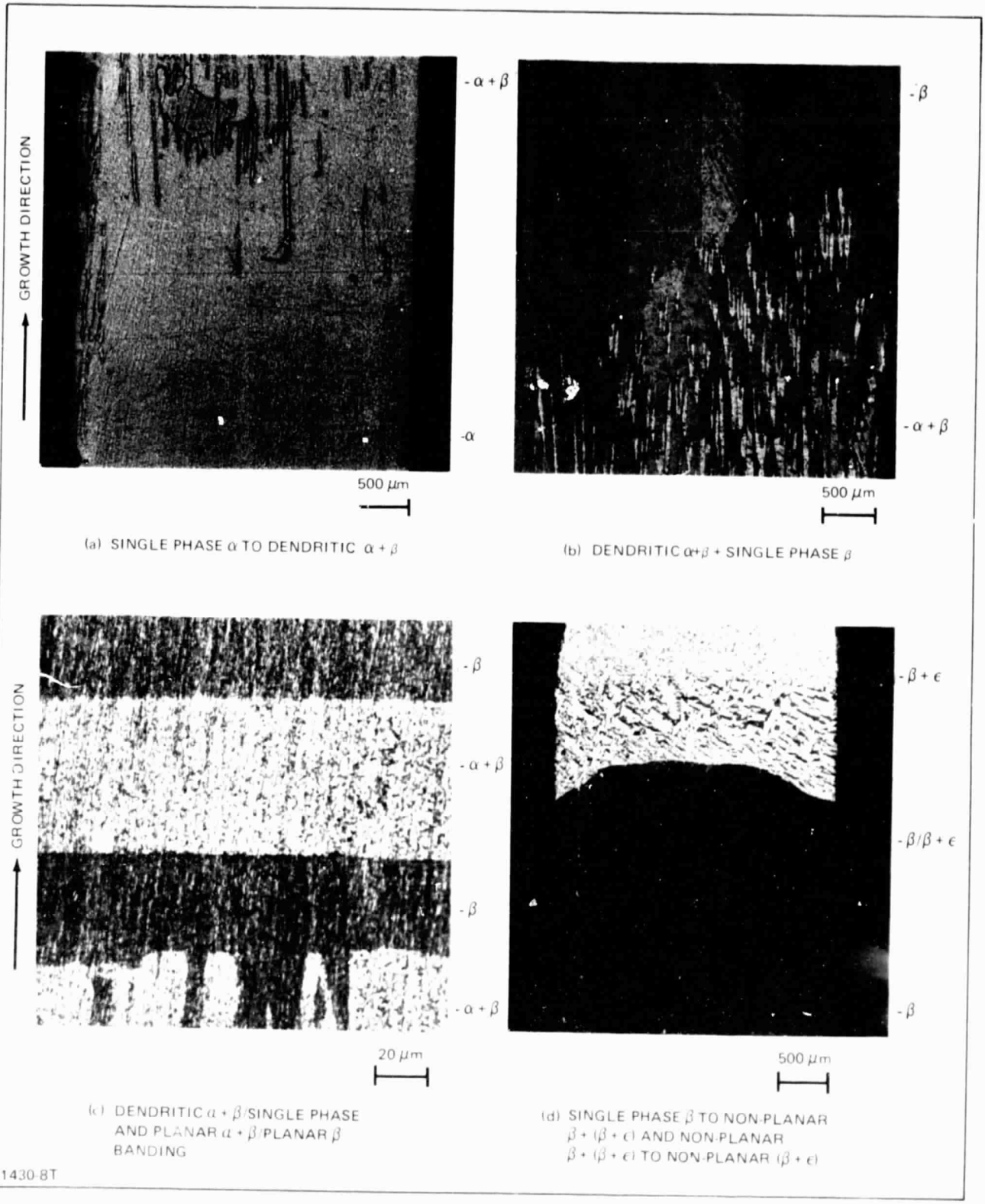

Figure 8 Pb-Bi Morphological Transitions for Directionally Solidified 28 Wt % Bi Alloy

This sequence can then repeat. This non-planar banding has not been reported previously in the literature. The next two bands are representative of planar banding, as previously reported in the literature. These structures were found in a sample that was processed with a G/V or $3.53 \times 10^6 \pm .76 \times 10^6$ °C s/cm^2. Lastly, the morphological transformations from planar β to non-planar off-eutectic $\beta + (\beta + \epsilon)$ solidification and subsequently from off-eutectic $\beta + (\beta + \epsilon)$ to eutectic $(\beta + \epsilon)$ are shown in Figure 8d. It should be noted that this eutectic does not solidify in a regular array. This is probably due to its reported doubly-faceted nature. This sample was solidified with a G/V of $5.28 \times 10^6 \pm .58 \times 10^6$ °C s/cm^2.

The calculated G/V requirements to avoid constitutional supercooling and concomitant spurious nucleation ahead of the solidification interface are shown in Figure 9 for the region of the Pb-Bi system of present interest (0-56 wt% Bi). These requirements were calculated using the liquid diffusion data of Savintsev and Rogov (Ref. 13) for eutectic Pb-Bi. This serves as a useful first-order approximation but neglects the compositional dependence of the diffusion coefficient. The experimental data are in agreement with the calculated results, particularly for the region of higher Bi concentration. The value of G/V was determined experimentally by in-situ measurement of the sample cooling rate and measurement of the furnace translation velocity.

The experimental results in the G/V regime, where entirely plane-front solidification was anticipated for hypoperitectic compositions, are more complex than expected. This may be seen in Figure 9. The morphological transformations that were noted were qualitatively similar to the planar properitectic α/ banded $\alpha + \beta$ and the planar peritectic β/ non-planar off-eutectic $\beta + (\beta + \epsilon)$ transitions shown in Figure 8. However, there were substantive quantitative differences. What appeared in the optical microscope to be single phase properitectic α was found to be supersaturated relative to the equilibrium terminal solid solubility (27.5 ± 1 wt % Bi), and x-ray analysis indicated an $\alpha + \beta$ two-phase mixture. This mixture was not evident optically, even at 2000-x, and scanning electron microscopy failed to develop sufficient phase contrast to show the microstructure at higher magnifications. (It is described as refined $\alpha + \beta$ in Figure 9. The formation mechanism could be either eutectic-like cooperative growth in a peritectic system, or the formation of a supersaturated α phase and

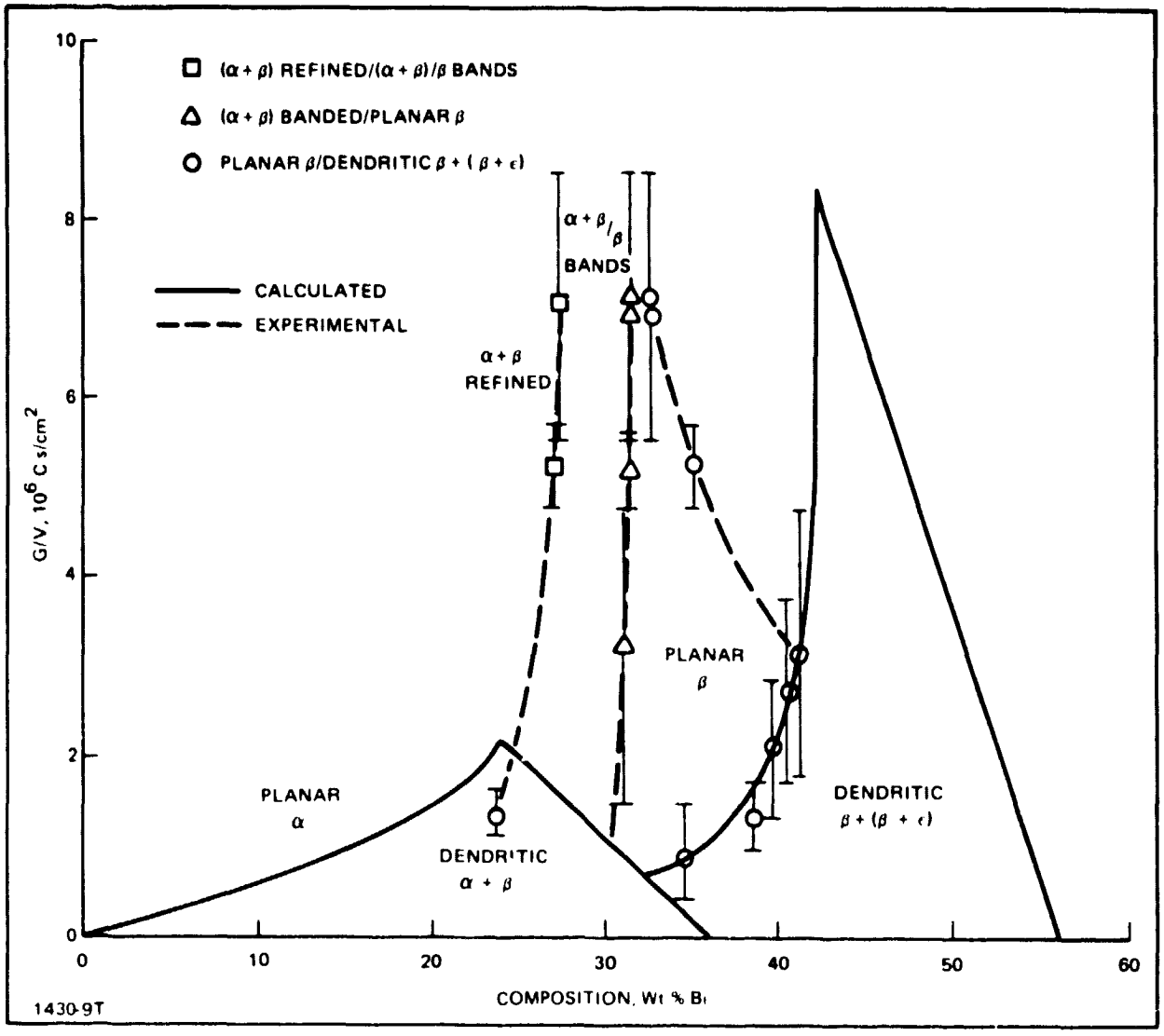

Figure 9 Calculated and Experimental Requirements for Morphological Stability

subsequent solid-state precipitation of the β phase. Characterization of this two-phase, refined, microstructure and identification of its formation mechanism are still in progress. The banded region comprised alternating bands of near constant composition.

The planar β to off-eutectic $\beta+(\beta+\epsilon)$ transition also provided a surprising result. At lower values of G/V, the maximum compositional extent of the β hyperperitectic phase field was described nicely by the constitutional supercooling criteria, as shown in Figure 9. However, as the G/V ratio is increased to $6.82 \times 10^6 \pm 1.51 \times 10^6$ °C s/cm^2, the extent of the β hyperperitectic phase field is greatly reduced. The reason for this reduction is uncertain at this time. One possible explanation is that a regime where morphological stability is limited by interaction with the convective flow field is encountered, rather than by the familiar constitutional supercooling (Ref. 14). This regime would be expected at low velocities. Since the primary means of achieving higher ratios of G/V was to hold the furnace conditions constant and lower the solidification velocity, this transition occurred only at the lowest velocities ($\leq$ 0.17 cm/hr).

Another interesting observation was that hyperperitectic β alloys exhibited refined two-phase $\beta+\epsilon$ microstructures which are shown in Figures 10a and b. It is believed that these two-phase microstructures are formed by solid state precipitation. At high temperatures (Figure 10a), precipitation consisted of a number of variants of, presumably, the same crystallographic precipitation system with elongated particles of ϵ dispersed in β. Nucleation at low temperatures (Figure 10b) consisted of heterogeneous nucleation of ϵ at the β grain boundaries.

3.1.3 Influence of Convection on Macrosegregation

A representative macrograph of a directionally solidified 32 ± 1 wt% Bi hyperperitectic alloy, solidified with a G/V ratio of $1.0 \times 10^6 \pm .21 \times 10^6$ °C s/cm^2, is shown in Figure 11. It is obvious that the constituent phases and the solidification morphology are significantly changing as a function of fraction solidified. Since the constituent phases vary widely in composition, this indicates that the local chemical composition varies significantly from end to end, i.e., macrosegregation.

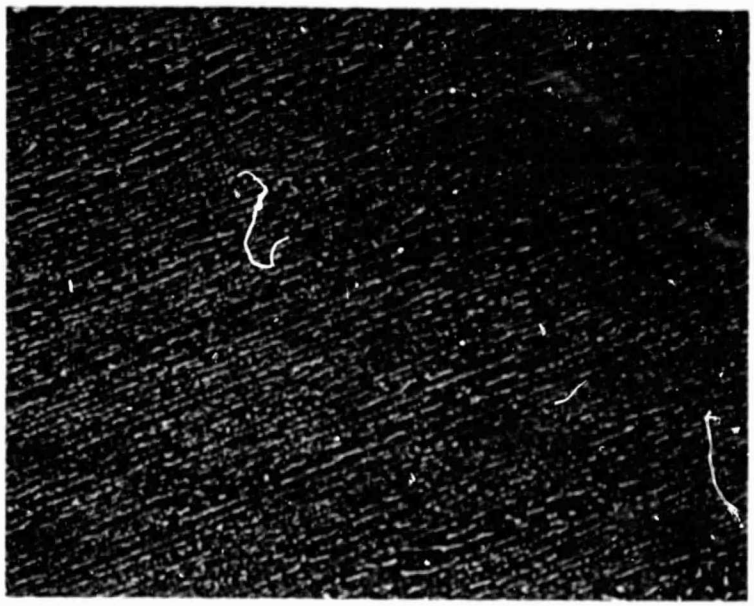

20 μm

GROWTH DIRECTION

a) HIGH-TEMPERATURE PRECIPITATION

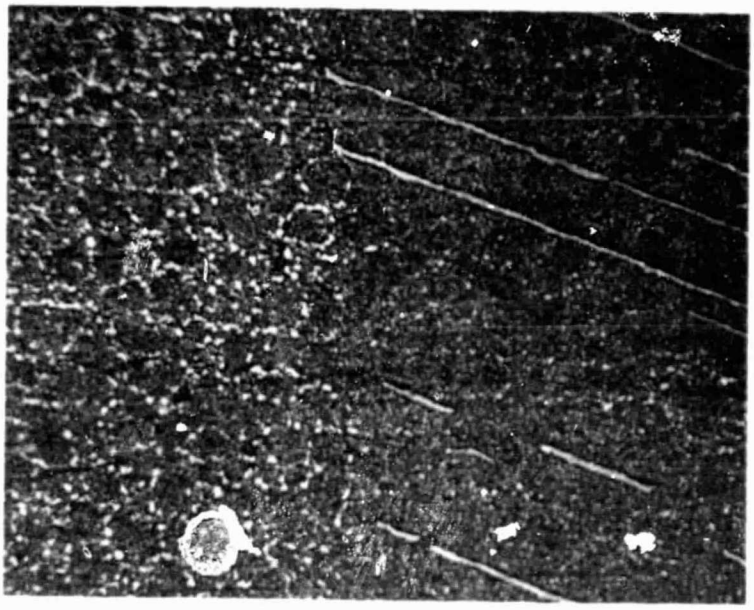

20 μm

GROWTH DIRECTION

b) LOW-TEMPERATURE PRECIPITATION

1470-10T

Figure 10 Solid State Precipitation of (in)

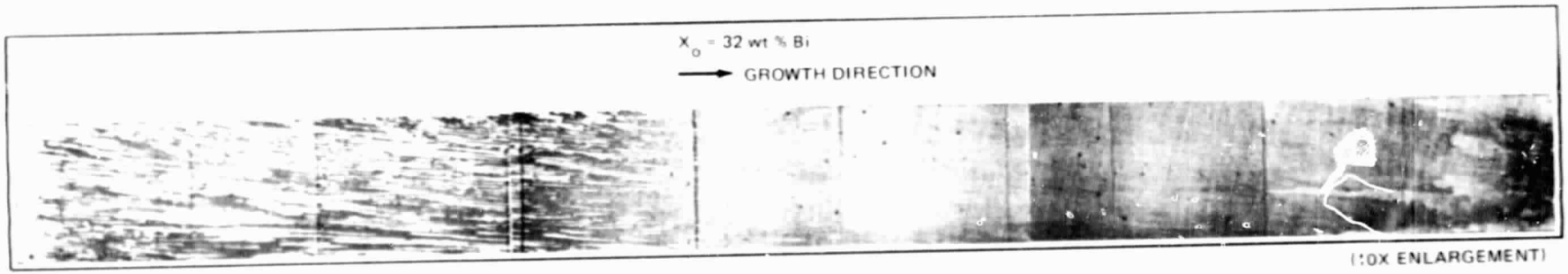

1430-11T

Figure 11 Optical Micrograph of a Directionally - Solidified 32 Wt % Bi Alloy Solidified at a G/V of 1.0×10^6 C s/cm^2

Macrosegregation can be due to interaction of the fluid convective flow field with the solute diffusional field in the liquid ahead of the solidification interface. The fluid convective flow field is usually described using a stagnant film where it is assumed that there is no mixing within a thin layer of thickness δ adjacent to the solidification interface and complete mixing in the liquid beyond δ . The stagnant film approach has resulted in models that have provided useful fits to experimental segregation data. When the stagnant film thickness is of the same order as, or less than, the solute diffusional boundary layer ahead of the solidification interface, then a non-steady state chemical redistribution occurs, resulting in chemical variation in the solid formed as a function of fraction solidified which is referred to as macrosegregation. The solute diffusional boundary layer is approximated by D/V, where D is the diffusion coefficient in the liquid. The more severe the overlap of the fluid convective flow field with the solute diffusional boundary layer, the more severe the macrosegregation will be. This overlap is given by the ratio of the stagnant film thickness δ to the solute diffusional boundary thickness D/V, or $V\delta/D$. When the ratio of $V\delta/D$ is $\ll 1$ it is considered a convective-controlled regime, and when the ratio is $\gg 1$ convection is thought to have little influence and solidification is diffusion-controlled. Macrosegregation due to convective mixing will be perturbed by the presence of Soret diffusion.

Microchemical analyses of the local composition vs. fraction solidified, for a 28 ± 1 wt% Bi hypoperitectic alloy directionally solidified at G/V ratio of $5.28 \times 10^6 \pm .58 \times 10^6$ °C s/cm^2, is shown in Figure 12. The sample microstructure in regions of morphological transition are superimposed on the diagram. Since the morphological transformations are assumed to occur isothermally, it would appear that changes in the liquid concentration at the solidification interface are largely responsible for these morphological transformations. Significant compositional variation was noted in all of the directionally solidified Pb-Bi alloys listed in Table 1. This was considered compelling evidence for convective-induced macrosegregation, which may have been augmented by Soret diffusion in the high gradient, low velocity, experiments. Compositional variations due to sample preparation were assumed to be small in this analysis.

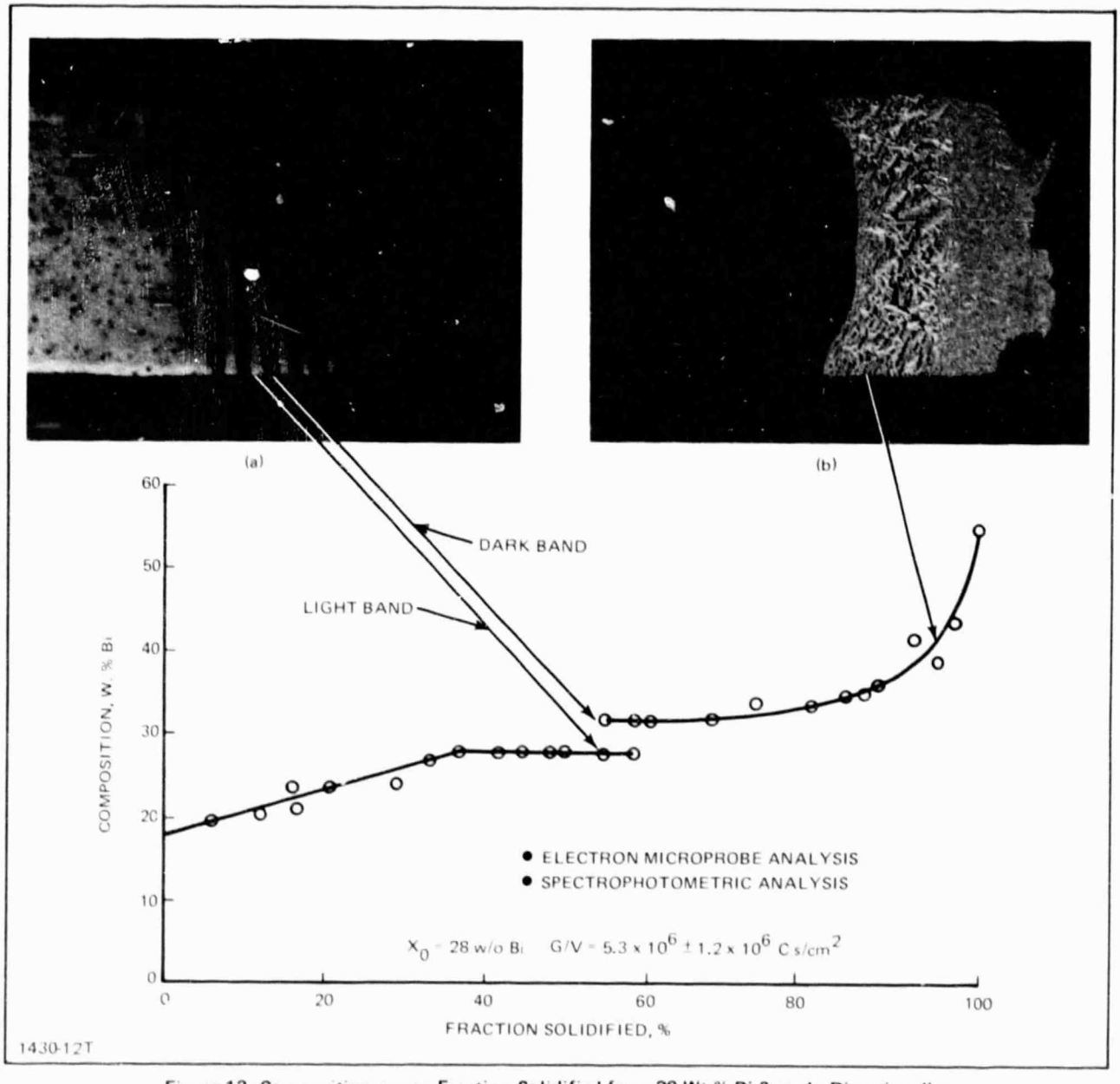

Figure 12 Composition versus Fraction Solidified for a 28 Wt % Bi Sample Directionally Solidified with G/V = 5.3 x 10^6 °C s/cm^2. Macrographs Showing the Morphological Transformations are Superimposed.

As a consequence of the experimental evidence indicating appreciable levels of macrosegregation for the Pb-Bi system, even in a thermally stabilized geometry, i.e., growth up, it was decided to develop a peritectic solidification model that considers peritectic solidification under conditions of partial mixing in the liquid ahead of the solidification interface.

This model is developed in the Appendix and gives equations for calculating concentration profiles resulting from directional solidification of melts that include a peritectic solidification reaction. Equations and calculated results are given for total mixing, partial mixing, and diffusion-controlled growth, for a planar interface at equilibrium. The model can account for planar morphological transitions demanded by compositional changes due to macrosegregation and phase relationships determined from the equilibrium phase diagram. It should be noted that the contribution of Soret diffusion to the macrosegregation is ignored. In view of the high thermal gradients and very low solidification velocities necessary to effect plane-front solidification in the Pb-Bi system, consideration of Soret diffusion would be worthwhile addition to the model.

A hypoperitectic melt composition, directionally solidified under partial mixing conditions, is predicted to follow this sequence (see Figure A-1): first, single phase properitectic α solidification, which continues until the peritectic liquidus composition is reached at the solidification interface; then two phase $\alpha + \beta$ solidification with the proportion of β increasing until single phase peritectic β solidifies; this continues until the eutectic liquidus composition is reached at the solidification interface when two-phase $\beta + (\beta + \epsilon)$ solidifies with the proportion eventually reaching the eutectic composition. This sequence of events is entirely consistent, qualitatively, with the morphological transformations noted experimentally and shown in Figures 11 and 12. Figures A-4 to A-8 illustrate the calculated influence of convection (partial mixing) on the composition vs. fraction solidified of a series of representative Pb-Bi alloys. Figure A-4 shows the macrosegregation anticipated for a nominal composition of 20 wt% Bi. This demonstrates that the greater the ratio of $V\delta/D$, the more uniform the composition will be as a function of fraction solidified. The experimental limitation of this conclusion is that the destabilizing solute gradients due to the rejection of Bi ahead of the solidification interface may limit us to a ratio of $V\delta/D < 1$ for all growth conditions, terrestrially.

Figure A-5 shows the results of similar calculations for a hypoperitectic alloy, 28 wt% Bi. In this case, the physical extent of the two-phase $\alpha + \beta$ region is strongly dependent on the level of partial mixing. Under diffusion-controlled conditions, hypoperitectic compositions would be expected to be almost totally two-phase. This was demonstrated in the literature by both Boettinger (Ref. 6) and Titchner and Spittle (Ref. 8), in Sn-Cd and Zn-Cu respectively, that did not have density destabilization in a thermally stabilized geometry, and hence no thermosolutal convection. The composition vs. fraction solidified curve in Figure 12, for a 28 wt% Bi-hypoperitectic alloy, is consistent with the high degree of mixing case ($V\delta/D \sim 0.1$). The initial, terminal, and extent of the banded two-phase field, are all consistent with the calculated results, although the composition at which the transition to the banded structure occurs differs significantly. The model output, therefore, is considered highly encouraging, at least for the hypoperitectic alloys that we are studying.

Figure A-6 shows the calculated results for a peritectic alloy composition, 30 wt% Bi. The conclusions of this study are consistent with those previously discussed. That is, to maximize the uniformity of the single-phase product, in this case peritectic β, or the extent of two-phase $\alpha + \beta$ solidification, the highest value of the ratio of $V\delta/D$ that can be experimentally achieved should be employed. Figure A-7 shows the calculated results for a hyperperitectic alloy, 35 wt% Bi, and the conclusions are similar to those previously reported.

Figure A-8 shows the fraction of two-phase $\alpha + \beta$ as a function of the ratio of $V\delta/D$ and bulk alloy composition. Clearly, to maximize the extent of this morphological regime, hypoperitectic compositions should be grown at the highest ratios of $V\delta/D$ experimentally possible. Similarly, since supersaturated compositions are the subject of investigation, compositions close to the supersaturated value anticipated and the highest ratio of $V\delta/D$ feasible should be employed.

3.1.4 Influence of Convection on Heat Transfer

During directional solidification, convection can also significantly influence heat transfer. This, in turn, can affect the location of the solidification interface, relative to the adiabatic zone of the Bridgman-Stockbarger furnace and the degree and character of mixing in the liquid ahead of the solidification interface. In considering the convective influence on heat transfer, both the heat

transfer to and from the ampoule, as well as heat transfer within the solid/liquid sample, must be taken into account. The contribution of convective heat transfer within the liquid is generally assumed to be negligible and theoretical calculations by Carlson (Ref 15) have shown this to be a good assumption both with respect to interface curvature and the thermal gradient in the liquid immediately ahead of the solidification interface. This greatly simplifies the heat transfer considerations at the solidification interface.

Experimentally, we have observed a convective influence. Thermal gradients in Pb 28 wt% Bi samples solidified vertically upward, in a thermally stabilized geometry, were found to be approximately twice those measured in samples grown vertically downward. This resulted in microstructures that were largely dendritic in the samples grown vertically downward due to a G/V ratio that was inadequate to stabilize plane-front solidification. This result seemed inconsistent with the previously cited theoretical results on the relative significance of convective heat transfer across the solidification interface, and experimental results that we have obtained in the eutectic Bi/MnBi system.

This unexpected result was explained by referring to a thermal model that was developed to describe the heat transfer during Bridgman-Stockbarger solidification (Ref. 16). Our furnace, described in Section 2.1.2, inputs heat to the ampoule and extracts heat from the ampoule across an air gap. In the thermally stabilized orientation (growth vertically upward), the air in the annular region between the ampoule and the furnace is also thermally stabilized. However, on inverting the system, to vary the growth direction relative to the gravity vector, the hot air in the annulus is in a bottom-most position and sets up a chimney effect, the hot air rising. This, in turn, changes the heat transfer coefficients at the heating and cooling zones of the furnace.

The thermal model of the Bridgman-Stockbarger furnace demonstrated that for some interface locations the thermal profile ahead of the solidification interface was particulary sensitive to the heat transfer coefficient in the cold zone of the furnace. Reduction of this coefficient due to the chimney effect initiated by inverting the furnace could thus significantly alter the thermal profile; that is, reduce the liquid thermal gradient, and translate the solidification interface further back in the chill block, introducing interface curvature.

The orientation effect is thus an effect of gravitationally driven convective heat transfer, but not one restricted to the heat transfer in the immediate vicinity of the solid/liquid interface. This effect can be minimized by locating the solidification interface close to the middle of the adiabatic zone of the furnace, as we have demonstrated in the Bi/Mn Bi eutectic system.

3.2 Sm-Co SYSTEM

3.2.1 Microstructural Analysis

Sm-Co samples of 20.2 ± 0.2, 14.1 ± 0.2 and 5.4 ± 0.2 a/o Sm have been fabricated using the induction melting techniques described in Section 2.2.1. These samples are representive of two-phase microstructures to be found in the $Sm_2Co_7/SmCo_5$, $SmCo_5/Sm_2Co_{17}$, and Sm_2Co_{17}/Co phase fields, respectively. The microstructure of a 5.4 ± 0.2 a/o Sm alloy is shown in Figure 13, with Sm_2Co_{17} dendrites within a Co matrix, as determined using magnetization and microprobe analysis.

In addition to optical microscopy, a powerful tool is being used to image the magnetic domain structure that involves the Kerr magneto-optical effect. Using plane-polarized light, we have been able to observe the magnetic domain structure of Sm_2Co_{17} regions within the domain structure of a Co matrix of a 5.4 ± 0.2 a/o Sm alloy as shown in Figure 14. It is at the phase interfaces (inhomogeneous magnetic surfaces) that reverse domains are thought to nucleate and limit the potentially large coercive fields of this class of materials (Ref. 17), since the magnetocrystalline anisotropy is strongly dependent on the local chemical composition, degree of order and the crystal structure. We will continue to investigate the use of the Kerr effect, as well as scanning electron microscopy (cyclotron effect) in the coming year. In addition, a closed-ampoule design for directional solidification will be evaluated.

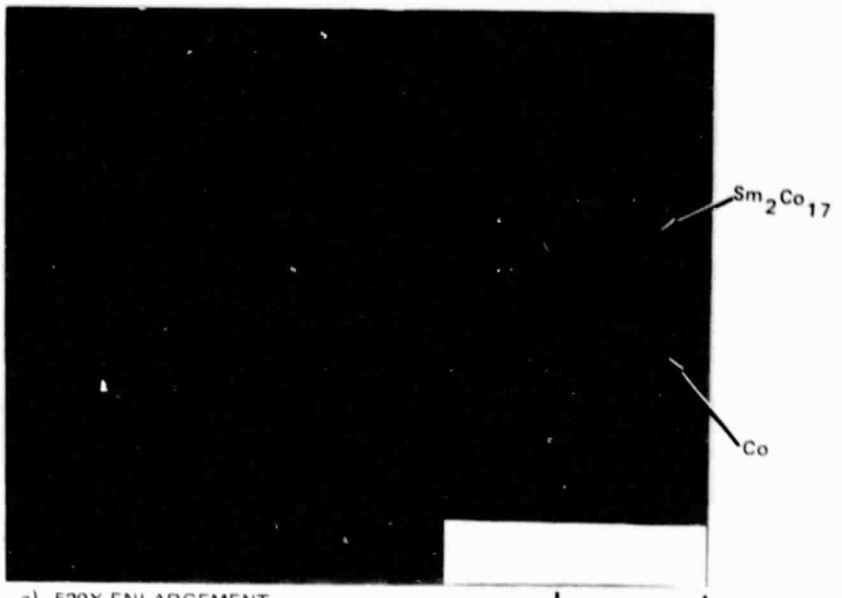

a) 520X ENLARGEMENT

50 μm

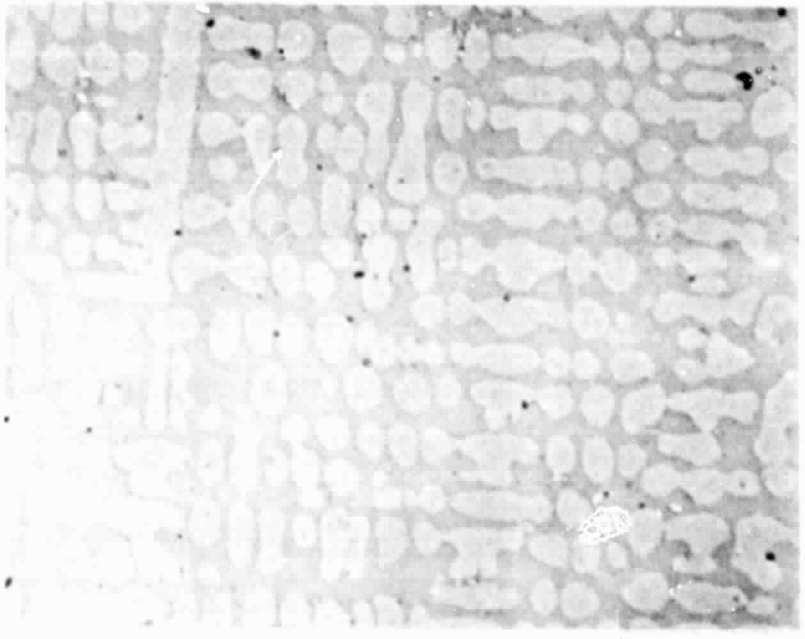

b) 60X ENLARGEMENT

100 μm

1430-14T

Figure 13 Representative Micrographs of Cast Sm_2Co_{17} in Co Matrix

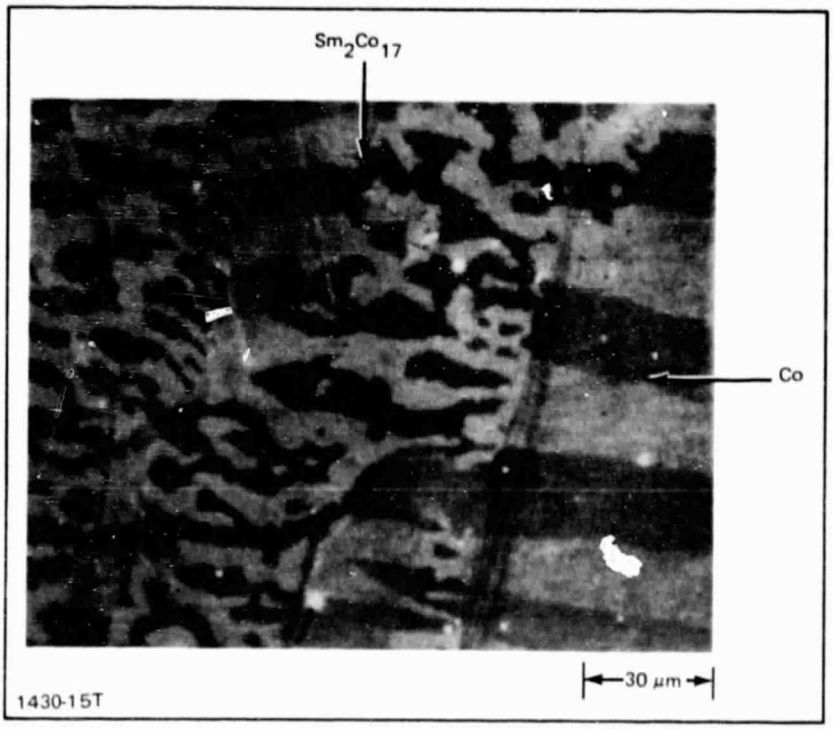

Figure 14 Domain Patterns of Sm_2Co_{17} Dendrites within Co Matrix for a 5.4 a/o Sm Alloy (650X)

4. SUMMARY AND FUTURE DIRECTION

Our experimental results generally verify the reported Pb - Bi phase diagram in the present region of interest.

The constitutional supercooling criteria offer reasonable upper limits for dendritic solidification. The high G/V experimental regime is the subject of continuing investigation.

Appreciable macrosegregation was noted during the directional solidification of all Pb-Bi alloys investigated and was attributed to thermosolutal convection and/or Soret diffusion. This pointed to the need for a peritectic solidification model that could account for partial mixing in the liquid ahead of the solidification interface. A candidate solidification model has been developed that offers qualitative agreement with the experimental results although it neglects Soret diffusion. Quantitative evaluation of the model will be conducted in the coming year, in the Pb-Bi system, and in the future in a system where solutally driven covection will oe damped in growth vertically upwards.

In addition to the influence of convective mixing on macrosegregation, influence of convection on heat transfer, for a Bridgman-Stockbarger geometry with an air gap, was found. The latter influence can be minimized by optimizing the location of the solidification interface within the adiabatic zone of the furnace.

Microstructurally refined hypoperitectic ($\alpha + \beta$) and hyperperitectic ($\beta + \epsilon$) compositions have been grown in the Pb-Bi peritectic system. The latter forms by solid state precipitation and the morphology may be due to the temperature of precipitation. The formation mechanism of the former is still under investigation.

Material handling, containment, processing, microstructural and magnetic characterization techniques for the Sm-Co system have been developed which will serve as a foundation for further work with this material. A closed ampoule has been developed which will eliminate the preferential loss of Sm and will allow directional solidification of Sm-Co peritectic alloys. Future work will determine whether microstructures grown in the Pb-Bi model system are observed in the Sm-Co peritectic systems and the influence of solidification processing and convective conditions on the microstructures and the magnetic properties of Sm-Co alloys.

5. REFERENCES

1. B. Chalmers: Physical Metallurgy, John Wiley & Sons, New York, pp. 271-72 (1959).
2. D.R. Uhlman and G.A. Chadwick: Acta Met., vol. 9, pp. 835-40 (1961).
3. B. Chalmers: Principles of Solidification, John Wiley & Sons, New York, pp. 224-27 (1964).
4. J.D. Livingston: Mat. Sci. Eng., vol. 7, pp. 61-70 (1971).
5. M.C. Flemings: Solidification Processing, McGraw-Hill, New York, pp. 117, 178 (1974).
6. W.J. Boettinger: Met. Trans., vol. 5, pp. 2023-2031 (1974).
7. K.A. Jackson and J.I. Hunt: Trans. TMS-AIME, vol. 236, pp. 1129-42 (1966).
8. A.P. Titchener and J.A. Spittle: Acta Met., vol. 23, pp. 497-502 (1975).
9. H.W. Kerr, J. Cisse, and G.F. Bolling: Acta Met., vol. 22, pp. 677-686 (1974).
10. G.I. Scherbakov, S.A. David, and M.D. Brody: Scripta Met., vol. 8, p. 1239-44 (1974).
11. B. Predel and W. Schwermann: Z. Metallk., vol. 58, P. 553 (1967).
12. J.F. Miller and A.E. Austin: J. Less-Common Metals, vol. 25 p. 317 (1971).
13. P.A. Savinstsev and V.I. Rogov, Zavod. Lab., vol. 35, No. 2, pp. 195-199 (1969).
14. W.J. Boettinger, S.R. Coriell, F.S. Biancaniello, and M.R. Cordes: Annual report on NASA Government Order M-27954B, NBSIR 79-1767, pp. 25-81 (1979).
15. F.M. Carlson: Unpublished research on "Convection Effects During Bridgman Growth of Semiconductors," NASA Research Grant NSG 1572, Clarkson College of Technology (1980).
16. T-W Fu and W.R. Wilcox: J. of Crystal Growth, vol. 48, pp. 416-24 (1980).

17. H. Kronmuller: 2nd Intl. Symp. Mag. Anis. and Coer., vol. 1, p. 1. (1978).

18. Buschow and Van der Goot, J. Less Common Metals, vol. 14, p. 323 (1978).

A-1. M. Zief and W.R. Wilcox, editors: Fractional Solidification, Dekker, N.Y. (1967).

A-2. W.R. Wilcox: J. Appl. Phys. vol. 35, p. 636, (1964).

A-3. J.D. Verhoeven and K.A. Heimes: J. Crystal Growth, vol. 15, p. 150, (1972).

A-4. P.S. Ravishankar and W.R. Wilcox: J. Crystal Growth, vol. 43, p. 480, (1978).

APPENDIX

SEGREGATION IN DIRECTIONAL SOLIDIFICATION OF PERITECTICS

INTRODUCTION

Equations will be developed here in order to calculate the expected composition vs. distance of directionally solidified peritectics for conditions of complete mixing, partial mixing, and no mixing. Partial mixing is treated using the ficititious stagnant film model, as discussed in the body of the report. The model suffers from the disadvantage that δ is unknown and must be found by comparison with experiment or by solution of the detailed partial differential equations for hydrodynamics and mass transfer.

In the treatments following, it is also assumed that complete equilibrium is maintained at the solid-liquid interface, and that the supercooling required to nucleate a new phase is infinitesimal. Thus we will find that, in the single-phase region, the solid and melt compositions are connected by a tieline on the phase diagram. At the peritectic point, however, both α and β phases are produced, with the amount of each determined by a material balance at the interface. This is exactly analogous to the situation for solidification of off-eutectic melts and, in fact, the differential equations and boundary conditions are identical in form.

In order to find any analytical solutions, it is necessary to make an assumption about the volumetric properties of the melt. In the following we have assumed that the density is independent of composition and temperature. While this is not exactly true, it makes for the simplest equations. If desired, we could make a more realistic assumption, i.e., that the partial molar volumes of both components are constant. In addition, the influence of Soret diffusion is ignored.

BASIC EQUATIONS

The schematic phase diagram shown in Figure A-1 serves to present graphically some of the symbols employed. These symbols are also defined in the table of nomenclature.

When the density of the melt is constant and no mixing is present, the differential equation for mass transfer in the melt is

$$D \frac{\partial^2 w}{\partial y^2} + V_{cf} \frac{\partial w}{\partial y} = \frac{\partial w}{\partial t} \qquad (A\text{-}1)$$

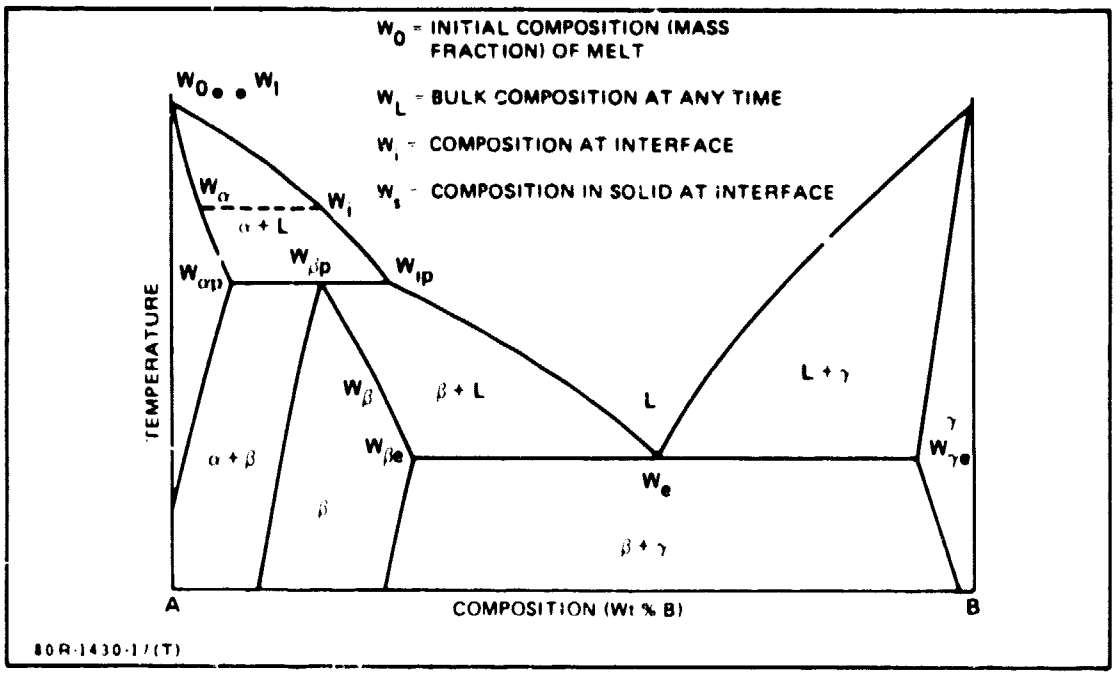

Figure A-1 Schematic Phase Diagram for Peritectic System

where D is the diffusion coefficient, w the mass fraction and y the distance from the interface. The term $V_{cf} = V\int \rho_s / \rho_\ell$ is the melt velocity toward the interface (taken as stationary), in which V_c is the linear freezing rate, ρ_s the density of the solid, and ρ_ℓ the density of the melt.

The initial boundary condition is

$$W = w_o \text{ at } t = 0 \tag{A-2}$$

and the material balance boundary condition at the freezing interface is

$$w_s V \rho_s = w_i V_{cf} \rho_\ell + D\rho_\ell \frac{dw}{dx} \text{ at } y = 0 \tag{A-3}$$

The boundary condition at the end of the ampul, z = L, is

$$\partial w/\partial y = 0$$

In the stagnant-film and complete-mixing models, we also require a material balance from freezing a small amount of melt in a finite charge,

$$w_s dg = d[w_\ell(1-g)] = (1-g)dw_\ell = w_\ell - w_\ell dg \tag{A-4}$$

where w_ℓ is the average composition of the melt. This can be integrated to

$$\int_{w_o}^{w_\ell(g)} \frac{dw_\ell}{w_\ell - w_s} = \int_o^g \frac{dg}{1-g} = \ln(1-g) \tag{A-5}$$

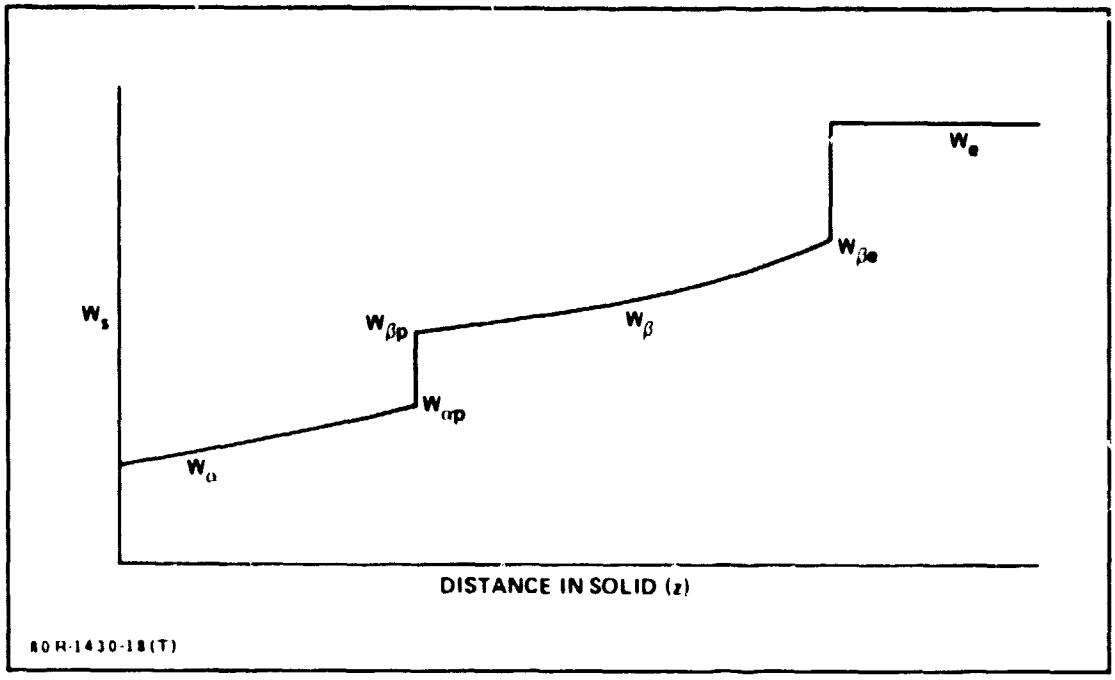

Figure A-2 Schematic Diagram of Redistribution for Complete Mixing

Thus, if w_ℓ is known as a function of w_s, we can obtain w_ℓ (and hence w_s) as a function of the mass fraction solidified, g.

COMPLETE MIXING

In this case $w_i = w_\ell$, and so w_ℓ and w_s are related by tielines. If $k = w_s/w_i$ is constant, then we may integrate Eq. A-5 to obtain the classic relationship for single phase solidification,

$$w_s = w_\alpha = k w_o (1-g)^{K-1} \qquad \text{(A-6)}$$

If $k \neq 1$, then Eq. A-5 must be integrated numerically.

This single-phase result is valid only until the liquid composition reaches the peritectic, w_{ip}. The solid composition then jumps immediately to the β phase composition, as shown in Figure A-2. When the melt composition reaches the eutectic, the solid jumps immediately to the eutectic composition.

PARTIAL MIXING

In the stagnant-film model, we assume the concetration profile is quasi-steady state, i.e. $\partial w/\partial t = 0$ in Eq. A-1. Consequently, the boundary condition of Eq. A-2 is unneeded. The boundary condition of Eq. A-4 is replaced by

$$w = w_\ell \text{ at } y = \delta \tag{A-7}$$

The general solution to Eqs. A-1, A-3 and A-7 is

$$w_s = \frac{w_\ell - w_i e^{-\delta V_{cf}/D}}{1 - e^{-\delta V_{cf}/D}} \tag{A-8}$$

In the single-phase region, w_s and w_i are related by a tieline. If we define the distribution (segregation) coefficient $k = w_s/w_i$, then Eq. A-8 becomes the well known Burton-Prim-Slichter equation,

$$k_{eff} \equiv \frac{w_s}{w_\ell} = \frac{k}{k + (1-k)e^{-\delta V_{cf}/D}} \tag{A-9}$$

If k, δ, V_{cf} and D are all constant, the substitution of Eq. A-9 into Eq. A-5 yields Eq. A-6 with k_{eff} substituted for k. If these are not constant, then again Eq. A-5 must be integrated numerically using Eq. A-9.

When the interfacial melt composition reaches the peritectic w_{ip}, β begins to solidify. Unlike the case of complete mixing, however, the solid composition does not jump immediately to $w_{\beta\rho}$. Both α and β solidify simultaneously (or in narrow bands), with the relative proportion varying to produce a concentration profile as shown in Figure A-3 for the Pb-Bi system ($k_\alpha = 2/3$, $k_\beta = 5/6$, $w_{\alpha\rho} = 0.24$, $w_{\beta\rho} = 0.30$, $w_{ip} = 0.36$). The relationship between w_s and w_ℓ is given by Eq. A-8 with $w_i = w_{ip}$.

If k_{eff} is constant in the single phase α region, then, from Eq. A-6, two-phase solidification begins when

$$w_s = w_{\alpha\rho} = kw_{i\rho} = k_{eff} w_o (1-g)^{k_{eff}-1} \tag{A-10}$$

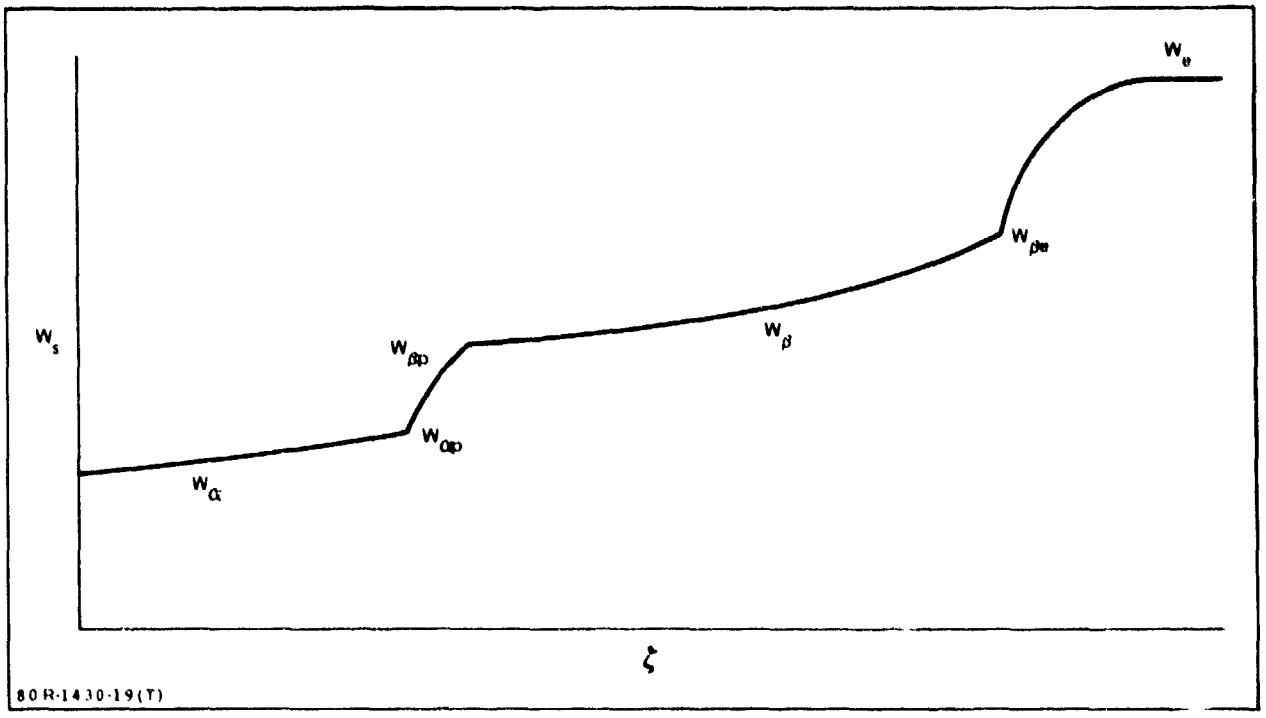

Figure A-3. Schematic Diagram of Redistribution for Partial Mixing

or, solving for g, when

$$g = 1 - (kw_{ip}/k_{eff}w_o)^{1/(k_{eff}-1)} \quad g_I \tag{A-11}$$

(If $g_I < 0$ then the solidification begins as two-phase $\alpha + \beta$).

The liquid composition at this point, g_I, is found by setting $w_s = kw_{ip}$ and $w_i = w_{ip}$ in Eq. A-8 to be

$$w_\ell = w_{ip}\left[k + (1-k)e^{-\delta V_{cf}/D}\right] \quad w_{\ell I} \tag{A-12}$$

The average composition in the two-phase region is then found by taking Eq. A-11 and A-12 as the initial conditions for Eq. A-5, integrating, and then substituting back into Eq. A-8

$$(w_s)_{avg} = w_{ip}\left\{1 - (1-k_\alpha)\left[\frac{1-g}{1-g_I}\right]^{(e^{\delta V_{cf}/D}-1)}\right\} \tag{A-13}$$

From the compositions of α and β at the peritectic, one can then easily calculate the fraction of each that is present. This two-phase solidification continues until

$(w_s)_{avg} = w_p$, and then single-phase β solidifies. By setting $w_s = w_{\beta p}$ in Eq. A-13, we obtain the point at which single-phase β begins to solidify:

$$g_{II} = 1-(1-g_I)\left[\frac{1-w_{\beta p}/w_{ip}}{1-k_\alpha}\right]^{(e^{\delta V_{cf}/D}-1)} \cdot \left[\frac{1-k_\beta}{1-k_\alpha}\right]^{(e^{\delta V_{cf}/D}-1)} \quad \text{(A-14)}$$

By substitution of $w_s = w_{\beta p}$ and $w_i = w_{ip}$ into Eq. A-8 to get w_ℓ, substituting this and Eq. A-14 into Eq. A-5 as boundary conditions, and then substituting this result back into Eq. A-8 we obtain the solid composition profile in the single-phase region:

$$w_s = w_{\beta p}\left(\frac{1-g}{1-g_{II}}\right)^{(k_{eff\,\beta}-1)} \quad \text{(A-15)}$$

The foregoing is true only if $g_I \geq 0$ in Eq. A-11. If $g_I \geq 0$ in Eq. A-11, then the initial solidification is two-phase $\alpha+\beta$. Noting that $w_i = w_{ip}$, we substitute for w_s from Eq. A-8 into Eq. A-5, and then substitute this back into Eq. A-8 to obtain the average solid composition in this two-phase region:

$$w_s = w_{ip} + \frac{w_o - w_{ip}}{1-e^{-\delta V_{cf}/D}}(1-g)^{(1/(e^{\delta V_{cf}/D}-1))} \quad \text{(A-16)}$$

This continues until $w_s = w_{\beta p}$, for which, from Eq. A-13,

$$g_{II} = 1-\left[\frac{w_{\beta p}-w_{ip}}{w_o-w_{ip}}(1-e^{-\delta V_{cf}/D})\right]^{(e^{\delta V_{cf}/D}-1)} \quad \text{(A-17)}$$

After this, single-phase β is produced according to Eq. A-15.

The interfacial composition reaches the eutectic at $w_s = w_{\beta e}$. Substitution of this into Eq. A-15 yields the condition terminating single-phase β and beginning two-phase $\beta+\gamma$:

$$g_e = 1-(1-g_{II})\left(\frac{w_{\beta e}}{w_{\beta p}}\right)^{(1-(k_{eff\,\beta}-1))} \quad \text{(A-18)}$$

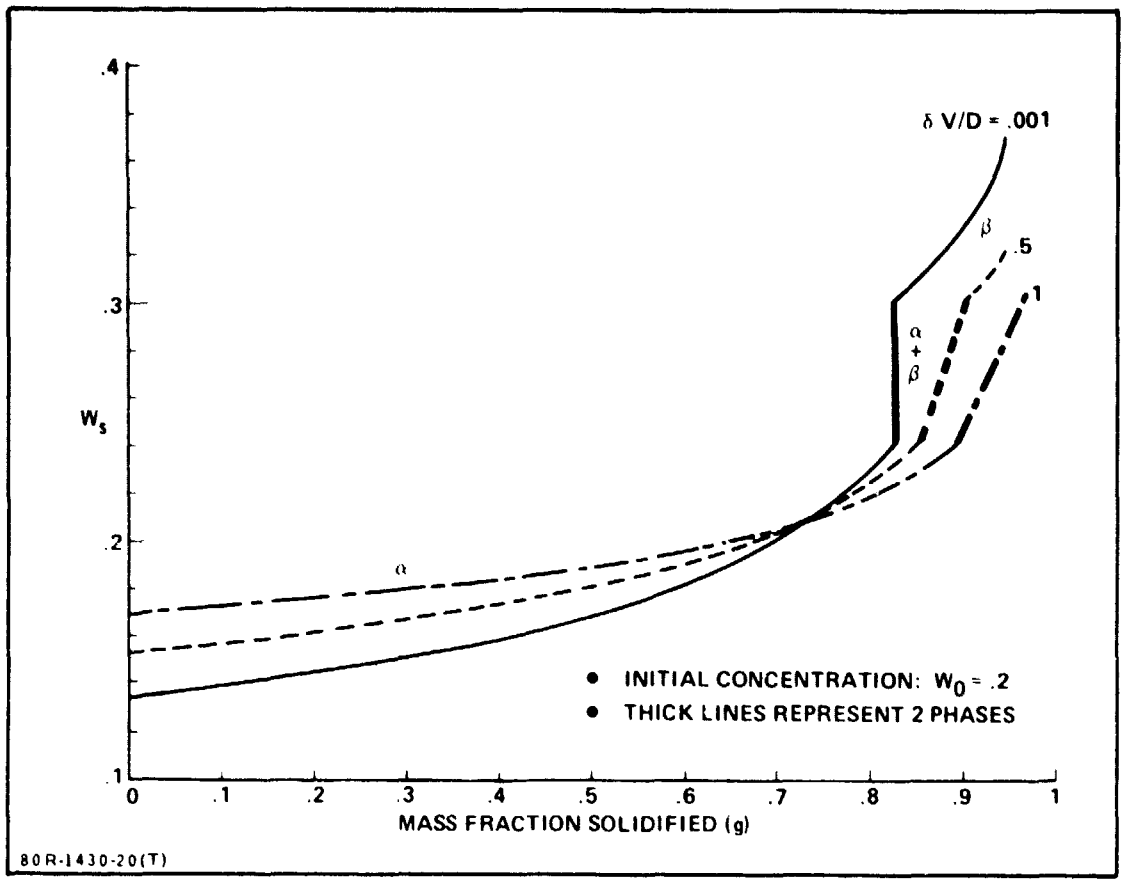

Figure A-4 Mass Fraction Bi for Directional Solidification of Pb-Bi Mixture Initially 20 Wt % Bi, as Function of $\delta V_{cf}/D$, for Partial Mixing of Melt

The subsequent solid is all two-phase $\beta + \gamma$, with average composition as expected for off-eutectic solidification (Refs. A-1 and A-2).

Figures A-4 through A-7 show results calculated for the Pb-Bi system. The mass fraction of the ingot predicted to be two-phase $\alpha + \beta$ is shown in Figure A-8 as a function of $\delta V_{cf}/D$ and of initial composition w_o. Note that virtually all of the ingot should be two-phase $\alpha + \beta$ when $w_o \sim (w_\alpha + w_{\beta p})/2$ and $\delta V_{cf}/D \gtrsim 1$.

It should be noted that an implicit assumption in the partial mixing stagnant-film approach is that δ be much less than the length of the melt. Thus, the high $\delta V_{cf}/D$ results can be valid only for large V_{cf} and not for large δ. When δ is on the order of the length of the container and $\delta V_{cf}/D \gtrsim 1$, it would be more valid to use the no-mixing results.

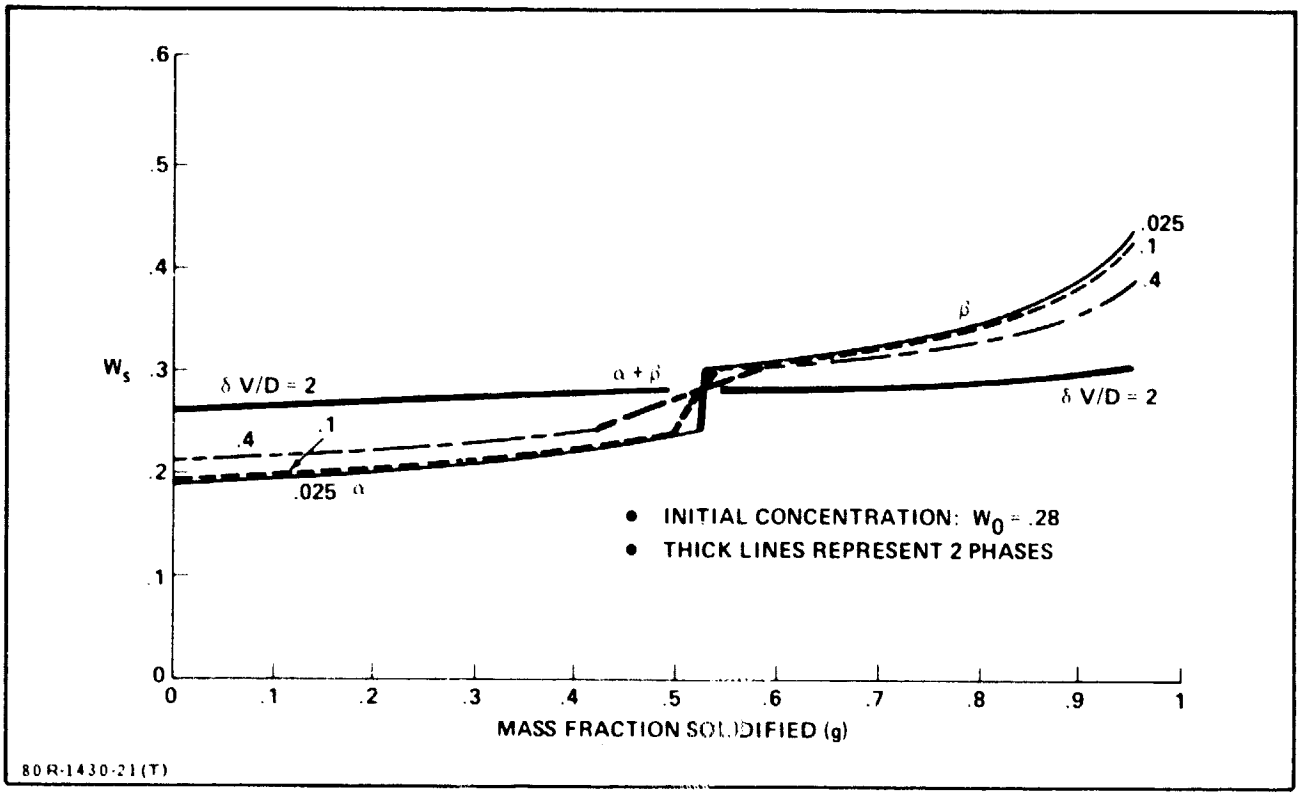

Figure A-5 Bismuth Concentration Profile for Initial Feed Composition of 28 wt % Bi in Pb

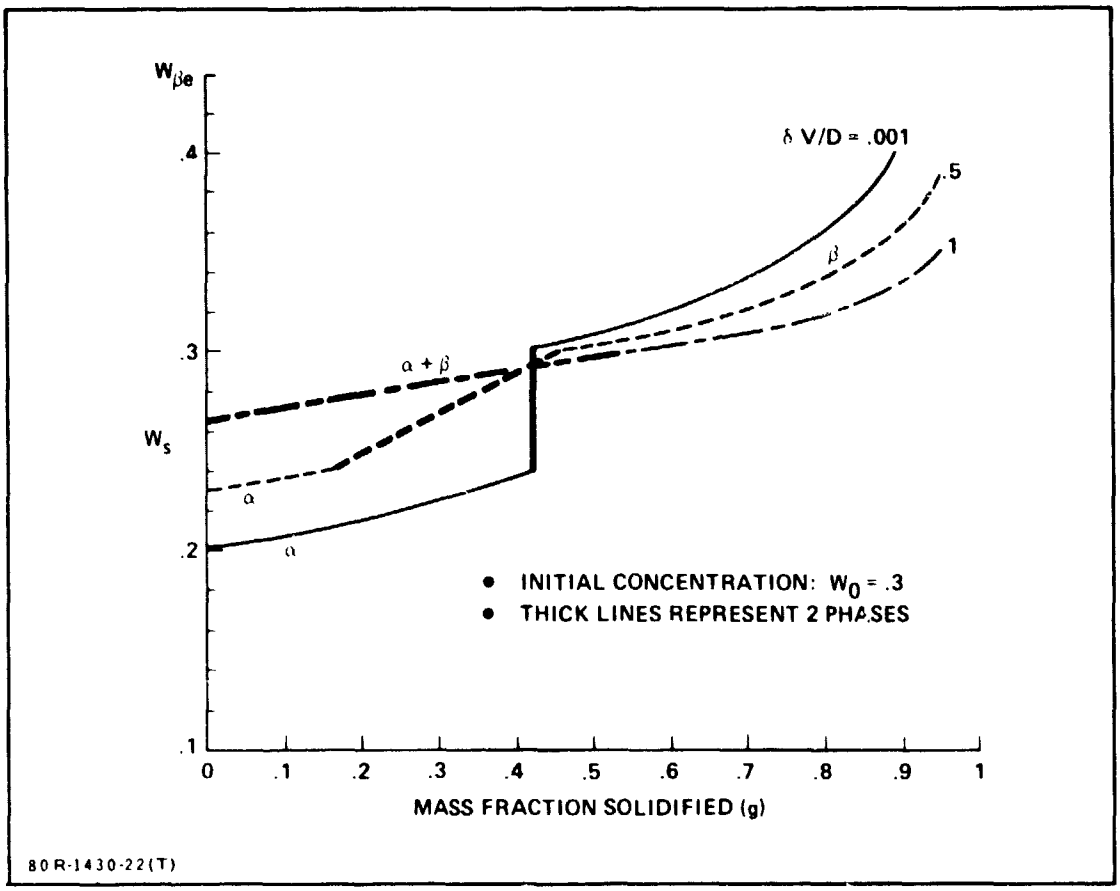

Figure A-6 Bismuth Concentration Profile for Initial Feed Composition of 30 Wt % Bi in Pb.

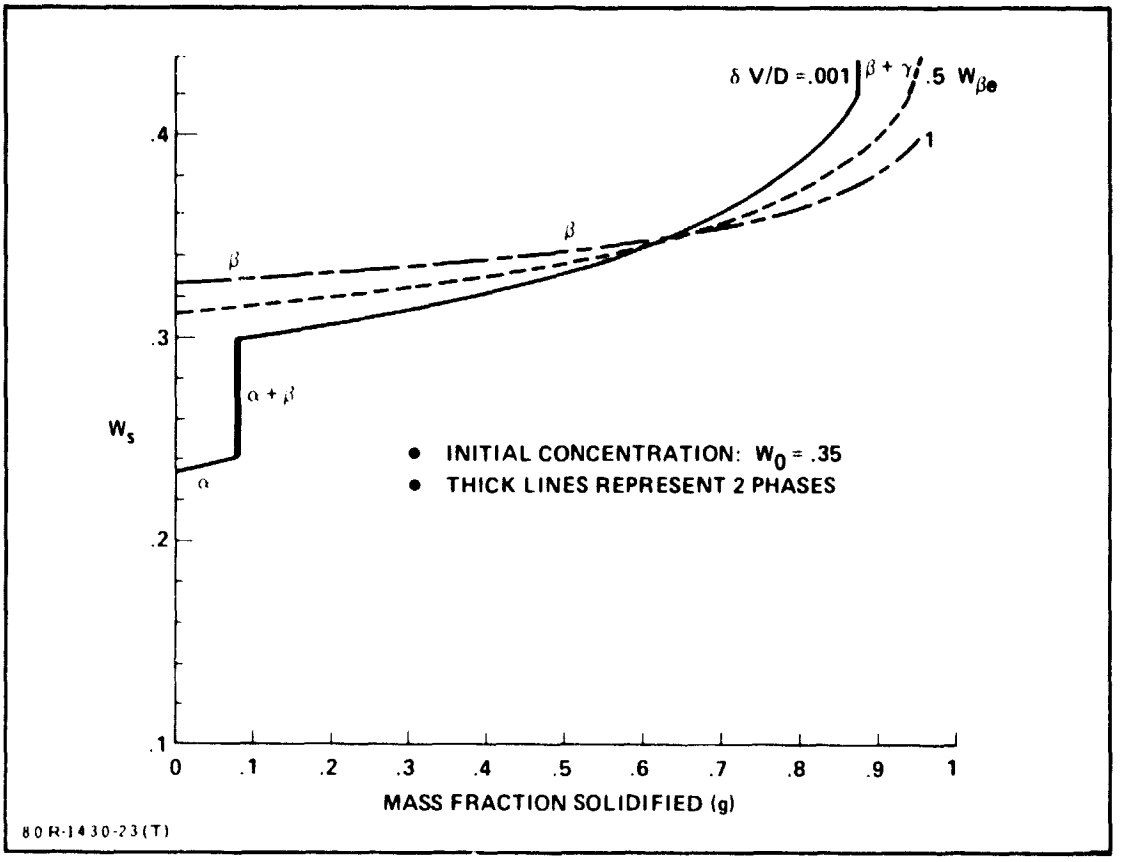

Figure A-7 Bismuth Concentration Profile for Initial Feed Composition of 35 Wt % Bi in Pb

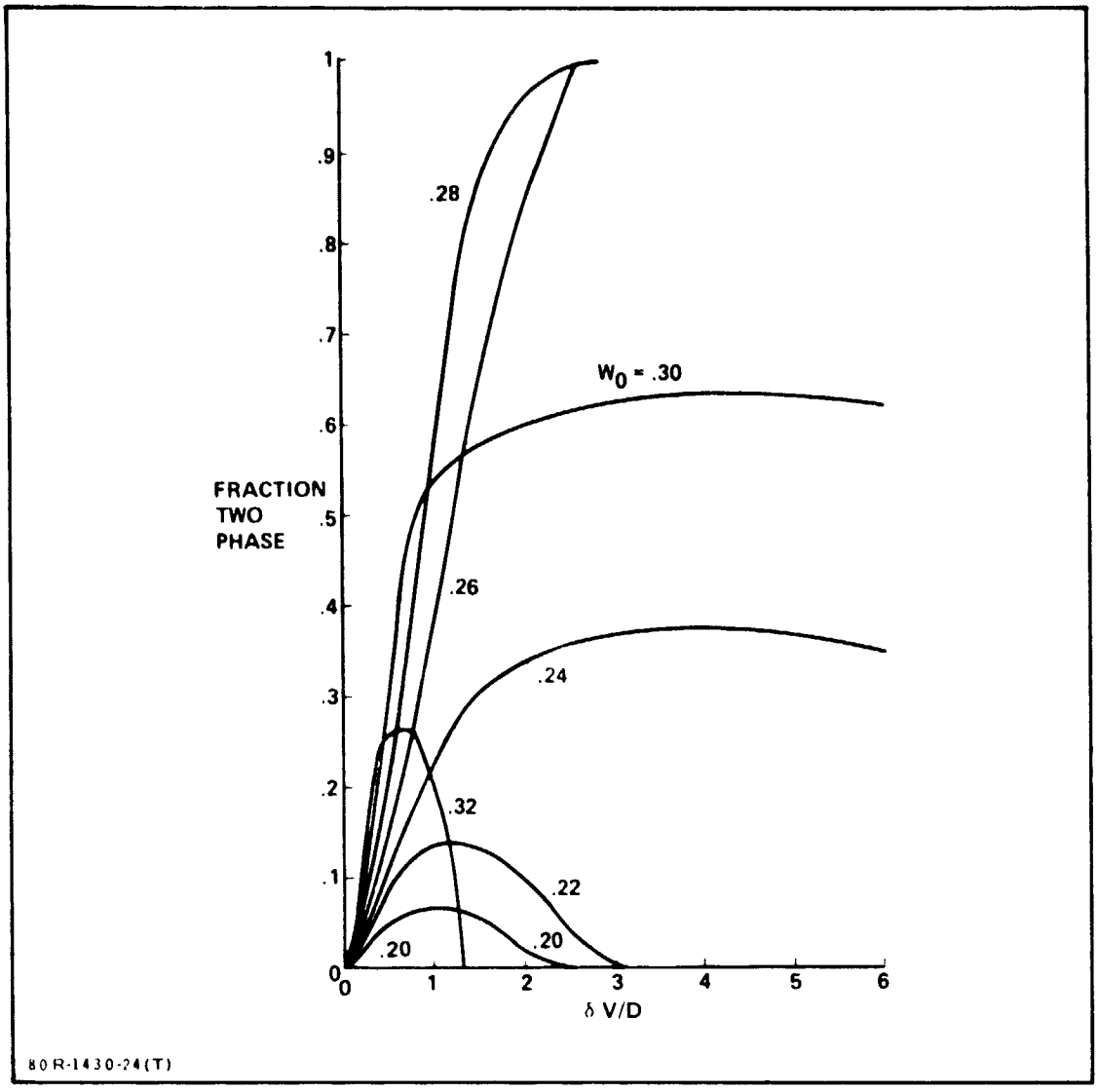

Figure A-8 Mass Fraction of Bi-Pb Ingots Predicted to be Two-Phase $\alpha + \beta$, as function of $\delta V_{cf}/D$ and Feed Composition

NO MIXING

No new solutions are required for pure diffusional mass transfer in solidification of peritectic systems, since the equations are identical to those used previously for single-phase solidification and for off-eutectic solidification.

In the single-phase region, numerical solutions to Eqs. A-1 to A-4 are required unless the distribution coefficient k is constant. For constant k, if the melt is much longer than the diffusion distance ($L \gg D/V_{cf}$), then the solution for an infinitely long ingot may be used,

$$w_s = w_\alpha = \frac{w_o}{2}\left\{1 + \text{erf}\left[\tfrac{1}{2}\left(\frac{zV_c}{D}\right)^{1/2}\frac{\rho_s}{\rho_\ell}\right] + (2k-1)\exp\left[-k(1-k)\left(\frac{zV_c}{D}\right)\left(\frac{\rho_s}{\rho_\ell}\right)^2\right]\right.$$
$$\left.\text{erfc}\left[\frac{2k-1}{2}\left(\frac{zV_c}{D}\right)^{1/2}\frac{\rho_s}{\rho_\ell}\right]\right\} \qquad \text{(A-19)}$$

where z is the distance down the rod.

Single-phase solidification continues, as shown in Figure A-9, $w_i = w_{ip} = w_\alpha/k_\alpha$. The value of $z = z_I$ at which this occurs must be found from Eq. A-19, most conveniently solved by plotting w_α/w_o vs. $(zV_c/D)(\rho_s/\rho_\ell)^2$ using the appropriate value of k.

When the peritectic composition is reached at the interface, two-phase solidification begins, as shown in Figure A-9. The equations are the same as for off-eutectic solidification, which unfortunately can only be solved approximately, and then only if k has been constant in the preceding single-phase regime. If $w_o \sim w_{ip}$, then the solution of Verhoeven and Heimes (Ref. A-3) is best. (Little two-phase material would be produced for $w_o \sim w_{ip}$.) For the more interesting case of $w_o \sim w_{\alpha p}$, the solution is (Ref. A-4).

$$(w_s)_{avg} = w_o - \frac{w_o - kw_{ip}}{2k}\left\{\text{erfc}\left[\tfrac{1}{2}\left(\frac{(z-z_I)V_c}{D}\right)^{1/2}\frac{\rho_s}{\rho_\ell}\right] + (2k-1)\exp\left[-k(1-k)\left(\frac{(z-z_I)V_c}{D}\right)\left(\frac{\rho_s}{\rho_\ell}\right)^2\right]\right.$$
$$\left.\text{erfc}\left[\frac{1-2k}{2}\left(\frac{(z-z_I)V_c}{D}\right)^{1/2}\frac{\rho_s}{\rho_\ell}\right]\right\} \qquad \text{(A-20)}$$

This is valid until $(w_s)_{avg} = w_{\beta p}$, after which single-phase β is produced. Since the above solution is already approximate, and since k is likely to vary widely during single-phase β solidification, it is unprofitable to seek an analytical solution in this region. A numerical solution would be necessary.

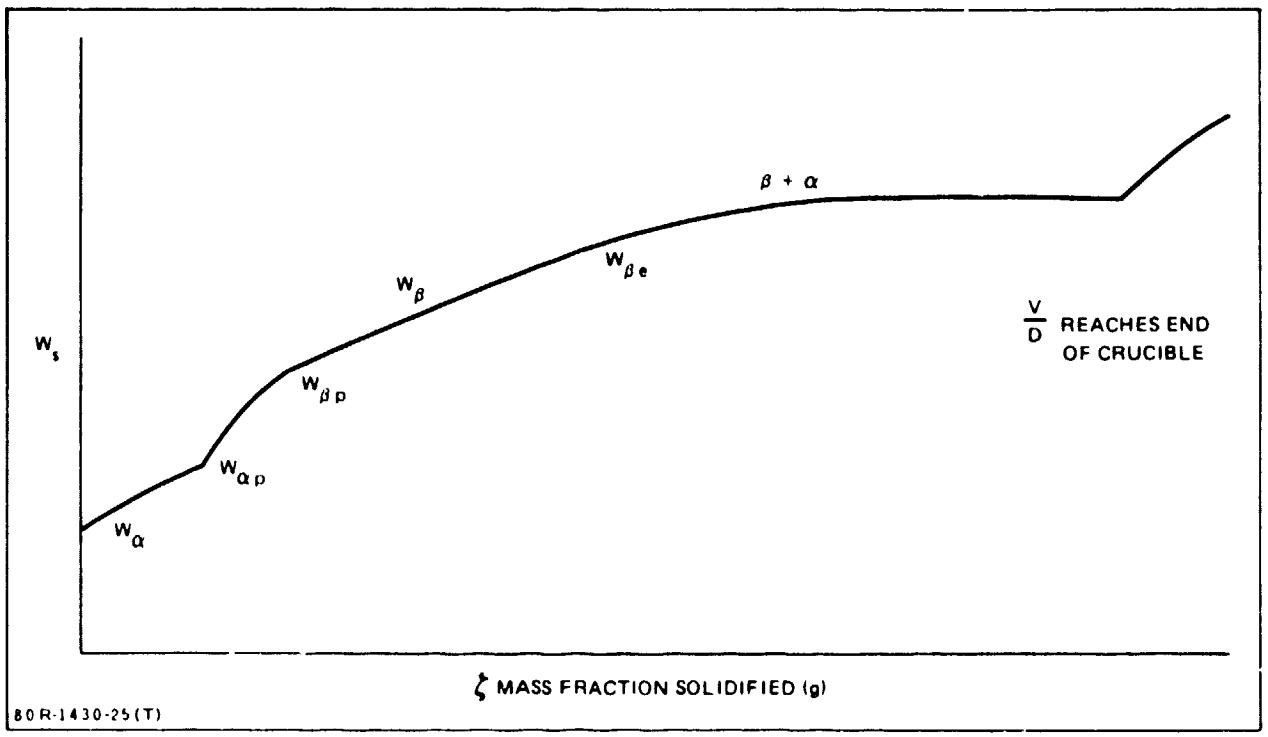

Figure A-9. Schematic Diagram of Concentration Profile for No Mixing in the Melt